

---

# Laboratory of Nuclear and Subnuclear Physics Measurements: Compton Scattering Experiment

A.Y. 2024/25



**Andrea Morandi 882695, Leonardo Stocco 868294  
Riccardo Bossi 881923**

---

## Abstract

This laboratory experiment investigates Compton scattering using a  $^{22}\text{Na}$  radioactive source, which emits back-to-back photons at 511 keV. One photon is used to trigger a coincidence gate, allowing the selective acquisition of events in which the other photon scatters off a copper target. The main objectives are to study the angular dependence of the scattered photon energy, to verify the Klein-Nishina cross-section formula, and to extract physical quantities such as the electron mass and its classical radius. The experimental setup includes two NaI(Tl) scintillation detectors: one for energy spectroscopy and one for coincidence gating. Calibration was performed using standard gamma sources to enable energy-to-channel conversion and to estimate detection efficiencies. The system geometry (distances, angles and target thickness) was optimized to balance resolution, statistical significance, and alignment constraints. Additional lead shielding was employed to suppress background from unscattered photons and to improve the signal-to-noise ratio. The electronic readout chain was carefully characterized and optimized, ensuring high energy resolution, stable timing and efficient coincidence detection. Spectra were acquired at various scattering angles in both transmission and reflection configurations. All simulation codes (including Monte Carlo and GeoGebra models), data analysis scripts, acquired spectra, experimental figures and final results are publicly available at: <https://github.com/oblivion0218/Compton>. This ensures full reproducibility and transparency of the methodology adopted throughout the experiment. *Several figures complementary to the explanations are included in Appendix F; readers are encouraged to refer to them for additional clarity.*

---

## Contents

<b>1 Electronic chain characterization</b>	<b>1</b>
1.1 Apparatus and readout electronics . . . . .	1
1.2 Resolution as a function of gain and tension . . . . .	1
1.3 Resolution as a function of shaping time . . . . .	3
1.4 Optimal conditions for spectrometer and gate . . . . .	4
<b>2 ADC linearity</b>	<b>5</b>
2.1 Apparatus . . . . .	6
2.2 Integral linearity . . . . .	6
2.3 Differential linearity . . . . .	6
2.4 Uncertainties and methodological review . . . . .	6
2.5 Conclusions about linearity . . . . .	7
<b>3 Coincidence techniques and stability</b>	<b>7</b>
3.1 Auto-coincidence . . . . .	7
3.1.1 Auto-coincidence spectrum . . . . .	8
3.2 Coincidence . . . . .	8
3.2.1 Coincidence spectrum . . . . .	8
3.3 Stability . . . . .	8
<b>4 Experimental set up</b>	<b>9</b>
4.1 Compton Scattering . . . . .	9
4.2 Alignment . . . . .	10
4.3 Target material selection . . . . .	11
4.4 Thickness . . . . .	11
4.5 Distances . . . . .	13
4.5.1 Spectrometer-target distance . . . . .	13
4.5.2 Gate-source distance . . . . .	13
4.5.3 Source-target distance . . . . .	14
4.6 Activity . . . . .	14
4.7 Efficiency . . . . .	15
4.8 Calibration . . . . .	15
<b>5 Measurements</b>	<b>16</b>
5.1 Shielding . . . . .	16
5.2 Energy spectra analysis . . . . .	16
5.3 Transmission measurements . . . . .	17
5.4 Reflection measurements . . . . .	17
<b>6 Cross Section Data Analysis</b>	<b>17</b>
6.1 Density of scattering centre . . . . .	17
6.2 Number of photons opening the gate . . . . .	18
6.3 Probability factor . . . . .	19
6.4 Spectrometer efficiency . . . . .	19
6.5 Detection solid angle . . . . .	19
<b>7 Results</b>	<b>20</b>
7.1 Measurement of the Electron Mass . . . . .	20
7.2 Measurements of the Classical Electron Radius . . . . .	20
<b>8 Uncertainties</b>	<b>22</b>
8.1 Rate uncertainties . . . . .	22
8.1.1 Statistical and systematic uncertainties . . . . .	22
8.1.2 $n_c$ and $\phi$ uncertainties . . . . .	25
8.1.3 $\epsilon_{spect}$ uncertainty . . . . .	25
8.1.4 $N_{gate}$ uncertainty . . . . .	25
8.1.5 $d\Omega_{spect}$ uncertainty . . . . .	26
8.1.6 Total uncertainties . . . . .	26

---

8.2	Angle uncertainties . . . . .	26
8.2.1	Peak shift uncertainty . . . . .	26
8.2.2	Scattering angle uncertainty . . . . .	27
8.2.3	Resolution uncertainty . . . . .	27
8.2.4	Statistical uncertainty . . . . .	27
8.2.5	Final results . . . . .	27
8.3	Energy uncertainties . . . . .	27
<b>9</b>	<b>Conclusion of the Experiment</b>	<b>27</b>
9.1	Main results . . . . .	27
9.2	Main experimental limits . . . . .	27
9.3	Future improvements . . . . .	28

## Appendices

<b>A</b>	<b>Scintillators</b>	<b>29</b>
<b>B</b>	<b>Compton Theory</b>	<b>29</b>
B.1	Compton Scattering . . . . .	29
B.2	Compton Cross-Section . . . . .	30
<b>C</b>	<b>Monte Carlo Simulation</b>	<b>30</b>
C.1	Photon Interaction Types . . . . .	30
C.2	Implemented cross-section . . . . .	31
C.2.1	Thomson scattering cross-section . . . . .	31
C.2.2	Photoelectric Effect cross-section . . . . .	31
C.2.3	Compton Scattering cross-section . . . . .	31
C.3	Interaction Probability and Attenuation . . . . .	31
C.3.1	Attenuation Factor . . . . .	31
C.3.2	Interaction Probability . . . . .	31
C.4	Comparison with NIST data . . . . .	32
<b>D</b>	<b>Relationship Between Cross-section and Count Rate</b>	<b>32</b>
D.1	Transmission . . . . .	32
D.2	Reflection . . . . .	32
<b>E</b>	<b>Optimal Thickness Calculation</b>	<b>33</b>
E.1	Transmission . . . . .	33
E.2	Reflection . . . . .	33
<b>F</b>	<b>Figures</b>	<b>33</b>
F.1	Electronic Chain . . . . .	33
F.2	Apparatus . . . . .	34
F.3	Measurements . . . . .	34
F.4	Compton Group . . . . .	34

---

## 1. Electronic chain characterization

This section briefly presents the first steps of the experiment, namely the characterisation of the apparatus. By this is meant the process by which it was possible to find the configuration that would allow the optimum values for energy resolution and position of the Compton peak to be obtained.

### 1.1. Apparatus and readout electronics

The electronic chain exploited for this experiment consists of various types of instrumentation, their functions are listed below:

- **Detector:**

Two NaI(Tl) scintillation detectors were employed during the experiment, each serving a specific purpose.

The first detector (*Ortec mod. 905-01, 1'' × 1''*[1]) was used to detect one of the two 511 keV annihilation photons emitted in opposite directions by the  $^{22}\text{Na}$  source. The resulting electrical signal is processed by a *differential discriminator*, which generates a *gate pulse*—a square wave that enables time-coincidence measurements with the second detector.

The second one (*SCIONIX mod. 51B51/2M, 2'' × 2''* [2]) was used for *spectroscopy* measurements. It detects the other 511 keV photon, which is scattered by a copper plate positioned between the source and the detector.

For further details on the operating principles of scintillation detectors, the reader is referred to Appendix A.

- **Preamplifier:** Both detectors are equipped with a preamplifier to provide initial amplification of the scintillation signal (*Ortec mod. 276, Photomultiplier Base with Preamplifier* [3]; *SCIONIX mod. VD14-E2, Preamplifier*[4]), without imparting any deliberate pulse-shaping to the current output.

- **Amplifier:** In order to form the signal coming out of the preamplifier a linear amplifier (*Ortec mod. 572* [5]) was used for the spectrometer, with different gain values and different options for shaping time. In particular, with regard to gain, the model used had, in addition to a knob allowing the gain to be varied from 20 to 1000, the possibility of inserting a damping factor of  $\times 0.1$ , which could be activated with a switch on the side of the amplifier. It was also possible to select the shaping time with which to form the impulse; the amplifier in fact had a further knob which allowed this parameter to be varied in a range between 0.5 and 10  $\mu\text{s}$ . An AMP-TSCA (*Ortec mod. 590A* [6]) was coupled to the gate, which in addition to signal

shaping could also function as a differential discriminator, capable of generating a gate pulse in the event of amplitude between two chosen values. Again, it was possible to select the gain level between 10 and 500 using a knob and the shaping time with a switch on the side of the module.

- **Reading electronics:** The electronics used to convert the signal from analogue to digital consists of an ADC (*Analog to Digital Converter*) and an MCA (*Multi-Channel Analyser*), both equipped inside the laboratory PC. [7]

- **Additional Components:** To power the two scintillators and their respective preamplifiers, a high-voltage power supply unit was used (*Caen Power Supply A7585* [8]).

In addition to the previously mentioned modules, two further components were included in the electronic chain:

- A Dual Timer module (*Caen N93B* [9]), used to delay logic signals in time.
- A NIM-TTL-NIM Converter (*Caen N89* [10]), employed to convert between logic standards, enabling proper communication between different modules.

For more details on the role of this additional component in the electronic setup, please refer to Section 3.1.

### 1.2. Resolution as a function of gain and tension

As far as the characterisation of the measuring apparatus is concerned, we started by analysing the resolution of the two detectors as a function of the gain imposed by the amplifier and the supply voltage of the photomultipliers connected to the NaI(Tl) scintillators.

The concept of energy resolution refers to the minimum energy range that the detector is capable of resolving. Let us consider a source that emits monoenergetic energy quanta. If a measuring apparatus had infinite energy resolution one would expect, as the counts increase, a differential spectrum assimilable to a Dirac delta centred in the energy value emitted, but this is not the case in reality; in fact, a Gaussian type spectrum is often recorded, which is more or less wide depending on the resolution of the detector taken into consideration. An operational definition of energy resolution can be expressed as follows, referring to Fig. 1.

In the figure, the energy resolution is expressed as the ratio of the *FWHM* (*Full Width at Half Maximum*), equal to  $2.35\sigma$  and the centroid  $H_0$  of the Gaussian. In a laboratory, there are several factors that can worsen the response of a detector. Among the most common are fluctuations in the operating

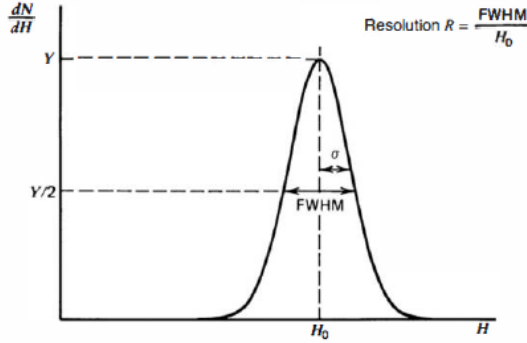


**Fig. 1:** Differential spectrum of a mono-energy source. [11]

characteristics of the system during the course of measurements, random noise sources inherent in the electronics of the system or statistical noise generated by the discrete nature of the measured signal.

Any photomultiplier requires an optimum voltage difference at the ends of the anode and cathode in order to operate efficiently; this is often provided by the manufacturer, who also indicates the upper and lower limits for this parameter. The need to define a range is due to the fact that if the voltage supplied to the photomultiplier were to be too low, the outgoing signal would be too weak, since most of the electrons generated at the photocathode would not be able to reach the first dynode, i.e. the first multiplication stage, affecting the linearity of the system and leading to a reduction in the sensitivity of the apparatus and a deterioration in the signal-to-noise ratio. On the other hand, an upper limit is provided in order not to damage the internal components of the photomultiplier in use, such as the photocathode and the dynodes inside it. Other risks related to the use of a supply voltage that is too high are the overheating of the apparatus, the increase in electronic noise and, lastly, the risk related to the generation of secondary electrons that can affect the sensitivity and linearity of the apparatus' response. The purpose of this first section was therefore to analyse how the response of the measuring apparatus varies as a function of the photomultiplier supply voltage in terms of energy resolution.

Analogously to the study performed on the voltage supplied to the photomultipliers, an investigation was carried out to determine the optimum gain to apply to the signal from the preamplifier. To do this, a linear amplifier (AMP) or, alternatively, an amplifier equipped with a time scanner (AMP-TSCA) was used, both of which are capable not only of giving a semi-Gaussian shaping to the signal, but also of adjusting the gain freely using a dedicated control knob. By varying this parameter, differ-

ential spectra are obtained that are approximately distributed over the 2048 channels of the available MCA as shown in the Fig. 2.

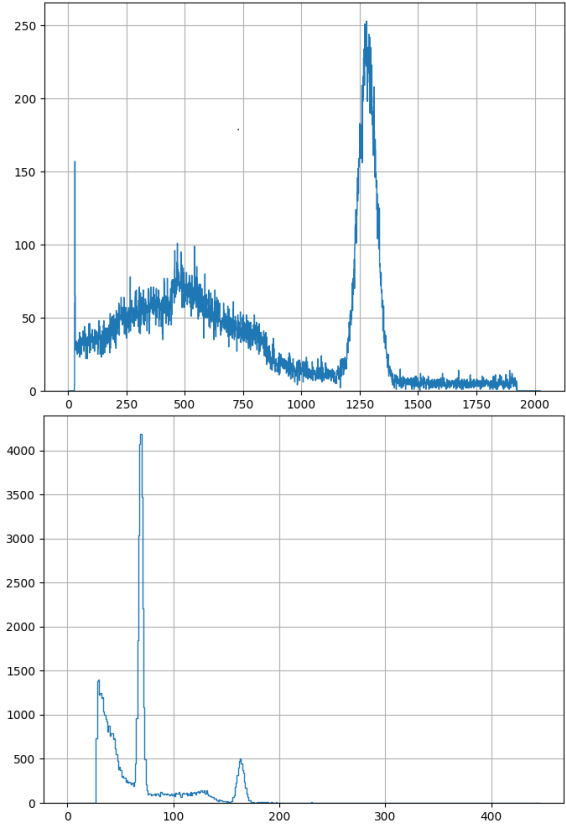


**Fig. 2:** Energy spectrum at varying amplifier gain: at the top a high gain plot is shown, while at the bottom a lower one is presented. The reported spectra are measured in MCA channels, as the apparatus had not yet been calibrated.

This made it possible to carry out an in-depth analysis of the energy resolution as the imposed gain varies.

Various spectra of  $^{22}\text{Na}$  were then sampled as gain and supply voltage varied.

In each case, a voltage value was always selected and for each one the spectrum was sampled as the gain varied.

A Gaussian interpolation (the background was also modelled in Section 5.2) centred on the 511 keV peak characteristic of  $^{22}\text{Na}$  was performed, and from this fit the data of the centroid  $H_0$  and the standard deviation  $\sigma$  matched to this distribution were extrapolated, which was then converted to the FWHM ( $FWHM = 2.35 \cdot \sigma$ ) to achieve the resolution for the peak. For all these interpolation plots, please refer to the GitHub link.

Using the formula in Fig. 1, it was then possible to calculate the energy resolution of each sampled

spectrum. The data was then represented with a heatmap (Fig. 3) in which the x-axis shows the supply voltage and the y-axis the gain; the values shown in the figure are the respective percentage energy resolutions.

In addition, other heatmaps were created (Fig. 4), which allowed the centroid of the Gaussian  $H_0$  to be reported as gain and supply voltage varied.

This is because in addition to taking into account the energy resolution, it was necessary to note how the spectrum was distributed over the channels of the MCA. In fact, for this experiment, 511 keV photons were used, which interact with a copper target via scattering with the electrons in the medium, this process leads to the observation of photons that are less energetic than the initial ones. Taking advantage of this information, an attempt was then made to centre the 511 keV peak in the second half of the MCA, avoiding positioning it in the channels between 1800 and 2048 because they would have been affected by the non-linearity of the apparatus (sec. 2). They then looked for configurations that could provide acceptable resolution and at the same time be able to meet the requirement of having  $H_0$  around channel 1400. Following this reasoning, we then found the optimum for Spectrometer and Gate, shown in Table 1.

Spectrometer was chosen to be paired with AMP, this because it is provided with a higher energy resolution and was used to perform spectroscopy measurements, while gate was fruitful to open the time window for coincidence measurements, it was then paired with the AMP-TSCA.

### 1.3. Resolution as a function of shaping time

The shaping time of a signal is a fundamental parameter when characterising a measurement apparatus. In fact, a signal coming from a generic preamplifier is characterised by a short rise time (time taken by the signal to go from 10% to 90% of maximum amplitude) and a long decay time, on the order of 50 – 100  $\mu\text{s}$ . This is not a problem when working with low count rates, but can cause pile-up when the frequency of events increases. To resolve this problem, in most cases an amplifier is inserted into the electronic chain to form the signal, so as to preserve the total amplitude of the signals coming out of the preamplifier and at the same time shorten their tails.

A further issue related to the choice of shaping time is the ballistic deficit, this phenomenon occurs when the pulse formation time is not sufficient to collect all the charges released by the interaction within the detector, leading to the recording of only a fraction of the original pulse, it is therefore essential to take this effect into account during

the shaping time selection process. As far as the amplifier is concerned, it has a crank that allows the shaping time value to be changed between 0.5 and 10  $\mu\text{s}$ , while the AMP-TSCA has a lever on the side that allows the user to choose between values of (0.5 – 1.5 – 3)  $\mu\text{s}$ . First we looked for the best signal-forming period, in terms of energy resolution, for the spectrometer, we then sampled several spectra of  $^{22}\text{Na}$  as this parameter varied and calculated the energy resolution for each. The results are shown in the figure 5.

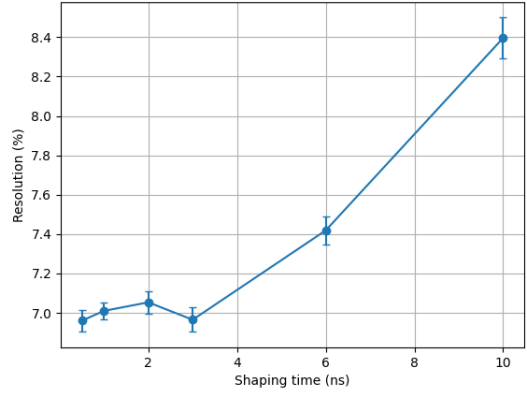
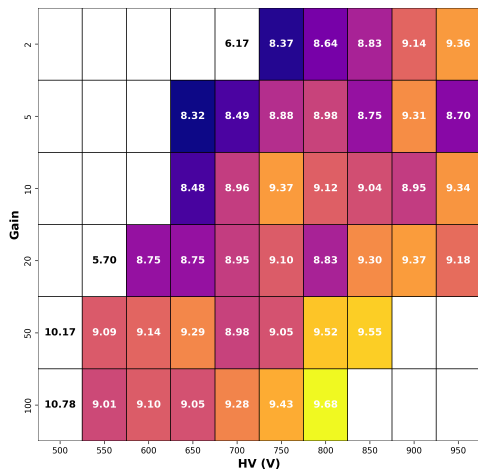


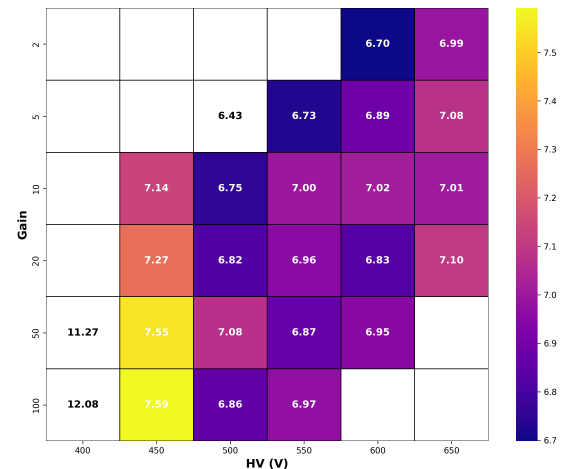
**Fig. 5:** Resolution values at varying shaping time for the spectrometer with AMP.

It can be seen from Fig. 5 that the energy resolution does not vary excessively for shaping time values between 0.5 and 3  $\mu\text{s}$ .

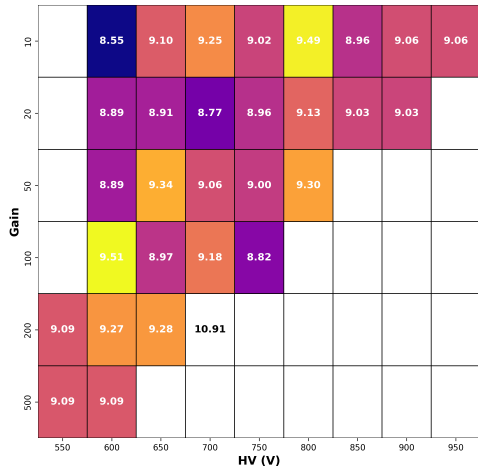
For the 0.5  $\mu\text{s}$  value, a shift in the Compton peak was noted, this effect is assumed to be due to a change in the amplifier's internal transfer function, it was therefore decided not to exploit this value as the total spectrum would be too 'squashed' in the first half of the MCA. The values of 2 and 3  $\mu\text{s}$  were also discarded for a different reason, as such a long signal time implied an increase in pile-up, which in turn required the source to be moved away from the detector, it was decided to discard these two options for purely geometrical reasons, as it would have required a source-spectrometer distance impractical in our laboratory. It was therefore decided to exploit a shaping time of 1  $\mu\text{s}$  for the spectrometer, a value which satisfies the requirements listed above to a good approximation. As far as the gate detector signal formation time is concerned, a different approach was followed, since only three values were available (corresponding to very similar energy resolutions), the ADC's request to first receive the gate signal and then that of the spectrometer was fundamental. The total processing time for the spectrometer can be expressed as:



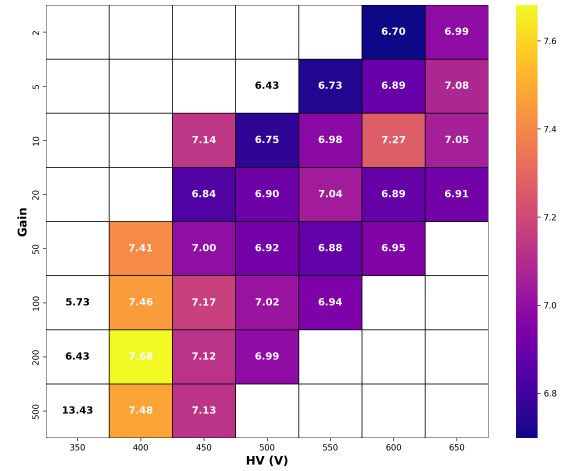
(a) Gate resolution with AMP.



(b) Spectrometer resolution with AMP.



(c) Gate resolution with AMP-TSCA.



(d) Spectrometer resolution with AMP-TSCA.

**Fig. 3:** Resolution as voltage and gain change.

$$\Delta t_{spectrometer} = 2.2 \cdot S.T. + 2 = 4.2 \mu s$$

Where  $2.2 \cdot S.T.$  is the time it takes for the semi-Gaussian signal leaving the amplifier to reach its maximum [11], while the additional factor 2 is an optional delay that can be added to the signal [5]. As far as the gate is concerned, the total time can be expressed as:

$$\Delta t_{gate} = 2.2 \cdot S.T. + 0.5 + 0.013 + 0.018 = 3.831 \mu s$$

where  $0.5 \mu s$  corresponds to the output of the signal from the AMP-TSCA [6],  $0.013 \mu s$  stands for the delay due to the signal passing inside the Dual Timer[9] while  $0.018 \mu s$  represents the delay associated with the signal transformation from NIM to TTL and vice versa ( $0.008 \mu s$  for NIM-TTL and

$0.01 \mu s$  for TTL-NIM, respectively [10]).

A signal forming time of  $1.5 \mu s$  was chosen due to the fact that  $0.5 \mu s$  did not allow for proper signal collection and  $3.0 \mu s$  would not allow for coincidence as required by the ADC.

#### 1.4. Optimal conditions for spectrometer and gate

In this section the optimal values chosen for voltage, gain and shaping time are presented; the resolution achieved by both scintillators along with the centroid of the peak at 511 keV are also shown in the Table 1 .

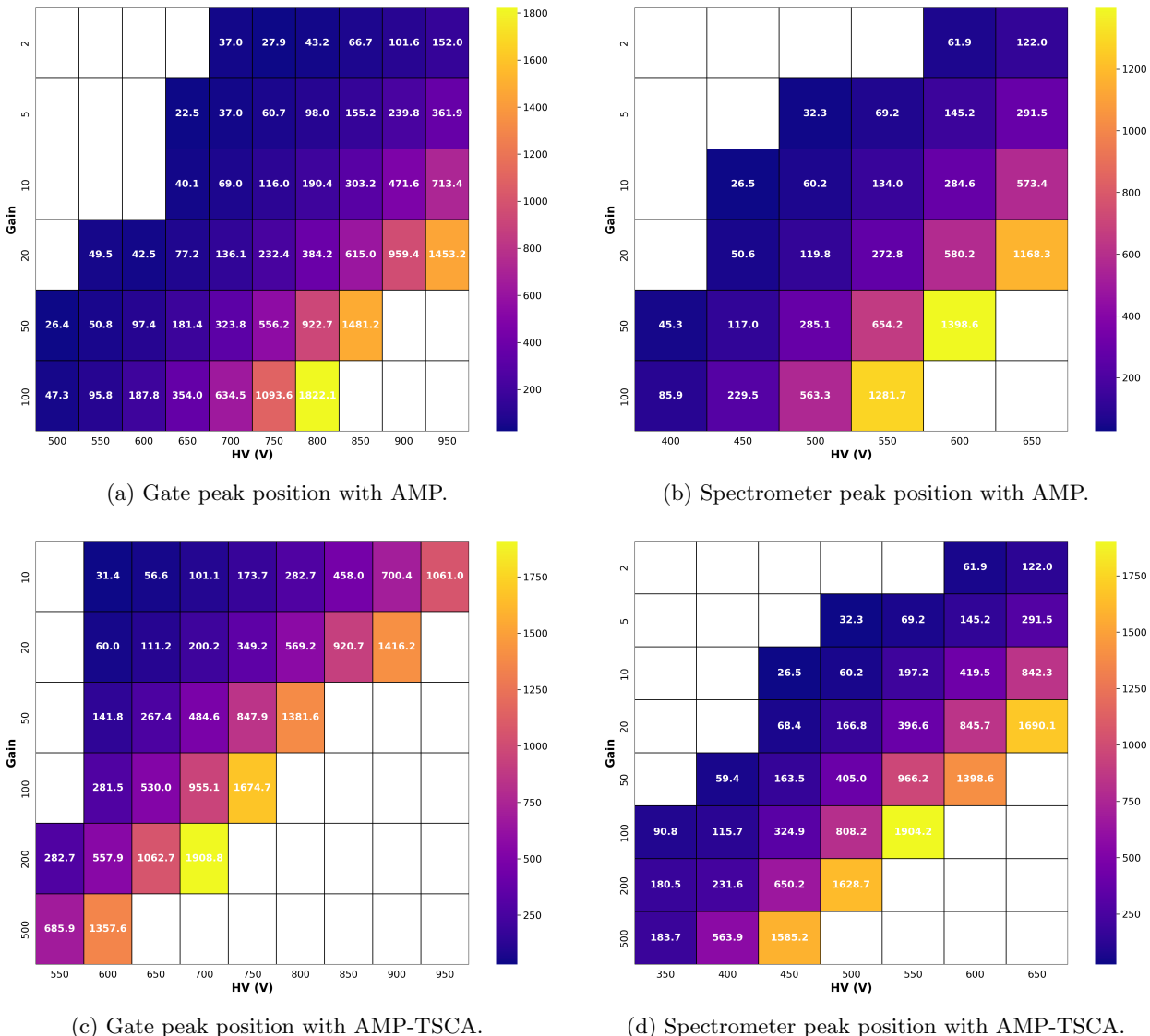


**Fig. 4:** Peak position as a function of voltage and gain.

**Table 1:** Values for the optimal configuration of the two detectors. The uncertainty linked to both resolution and channel is  $\sim 1\%$ .

	Voltage (V)	Gain	S.T. ( $\mu s$ )	Resolution	Ch.
Gate with AMP-TSCA	900	20	1.5	9.03 %	1416
Spectrometer with AMP	600	50	1	6.95 %	1398

## 2. ADC linearity

An ADC is a device used to convert a signal from analog to digital. However, like any electronic instrument, it can exhibit non-linearities that change its behaviour from the ideal scenario. In this section the evaluation of these discrepancies is presented. The ADC cooperates with another module, the MCA, whose job is to collect the values supplied

to it and produce a histogram. In the configuration available in the laboratory, the MCA and ADC are integrated within an electronic board located directly in the PC case. Therefore, the non-linearities of these two modules must necessarily be analysed together.

---

## 2.1. Apparatus

From the manual [7], it appears that the supplied ADC is designed to analyse pulses with semi-Gaussian shaping. These pulses can be obtained by using a pulser and passing the signal through both the preamplifier and the amplifier (or AMP-TSCA). However, this configuration introduces additional electronic noise and distortion due to the increased complexity and length of the electronic chain. An alternative is the use of an additional module, the pulse generator, which can deliver pulses with manually selectable rise ( $t_{rise}$ ) and decay ( $t_{decay}$ ) times. Semi-Gaussian shaping can be achieved by imposing equal values for the two characteristic times. After several attempts, it was found that setting both times to  $0.5 \mu\text{s}$  yields the maximum voltage attainable by the instrument, which is about 7 V.

However, this procedure posed a problem since the ADC is designed to sample pulses with a maximum amplitude of 10 V (under some conditions, up to 12 V) [7]. A possible solution would be to avoid the use of semi-Gaussian shaping by providing the ADC with a long-tailed exponential signal, but, even in such configuration, 10 V could not be exceeded. To overcome this limitation, it was decided to supply the signal produced to the amplifier in a semi-Gaussian formatting, allowing the amplitude to be chosen in voltage.

AMP rather than AMP-TSCA was chosen because the manufacturer guarantees non-linearities of less than 0.05% (with an optimal shaping time of  $2 \mu\text{s}$ ), which are still lower than those claimed for the ADC. [7]

Finally, pulse frequency was considered. Too high frequencies exacerbate the pile-up phenomenon and compromise the analysis, making it impossible to isolate the single bin, resulting in signal broadening to adjacent bins. Therefore, the lowest possible frequency of 25 Hz was chosen, both to reduce pile-up and for reasons of instrumental accuracy; for a more detailed discussion, see the dedicated section (Section 2.4).

## 2.2. Integral linearity

Integral linearity represents the maximum deviation from the ideal relationship between applied voltage and associated channel. In a perfect system an increase in voltage results in a proportional increase in the associated channel. In the real case, however, the channels of the ADC are discrete, and for voltage increases that are too small, the transition to the next channel is not observed. This phenomenon produces the typical stepped pattern of the conversion graph.

In the present study, the minimum voltage incre-

ment was chosen so as to allow sampling of one bin at a time, thus avoiding the phenomenon whereby, as the voltage increases, the system remains in the same bin.

In addition, deviation from linearity is expected at the extremes of the readout scale: for voltages that are too low, the signal may be distorted and difficult to read; for voltages that are too high, the system may become saturated or exhibit distortion, resulting in non-linear behaviour.

In practice, thanks to the pulse generator, the low-voltage zone was sampled with higher point density. Subsequently, a larger pitch was chosen for the middle zone, while, near the voltage limit, finer sampling was again adopted.

The interpolation lines show a clear linear behaviour within the analysed ranges, but exhibit a reciprocal offset, visible in Fig. 6. This is due to the different configuration of the electronic chain used in each case. In fact, each chain introduces its own gain and offset, which are reflected in the different positioning of the curves, while maintaining the linearity of the system.

## 2.3. Differential linearity

Differential linearity evaluates the combined response of MCA and ADC for each channel as the input energy is varied. With a fixed frequency for signal production, it is known a priori how many pulses are produced, so it is expected that the same number of counts will be observed in each channel. However, real ADCs exhibit an optimal operating zone for the central channels, with degraded performance at the extremes. Consequently, a maximum number of counts is expected in the central zone and a decreasing number toward the edges.

For this test, a frequency of 25 Hz was used (see the section 2.4 for more details) and an acquisition time of 10 seconds. With these settings, data were collected in all bins, from the lowest values up to channel 2000. Beyond this threshold, the recorded values were no longer significant.

## 2.4. Uncertainties and methodological review

The choice of the 25 Hz frequency was motivated by both the need to minimize pile-up and the goal of minimizing uncertainty on counts. With an acquisition time of 10 seconds, an attempt was made to ensure that no additional counts occurred in the time it took for the acquisition to stop, thus justifying the assignment of an error on counts of  $\pm 1$ . As for channel and voltage, different errors were adopted: for voltage, the oscilloscope instrumental error was used, while for channel, the error associated with a uniform distribution was referred to. Finally, in some situations, counts were spread over

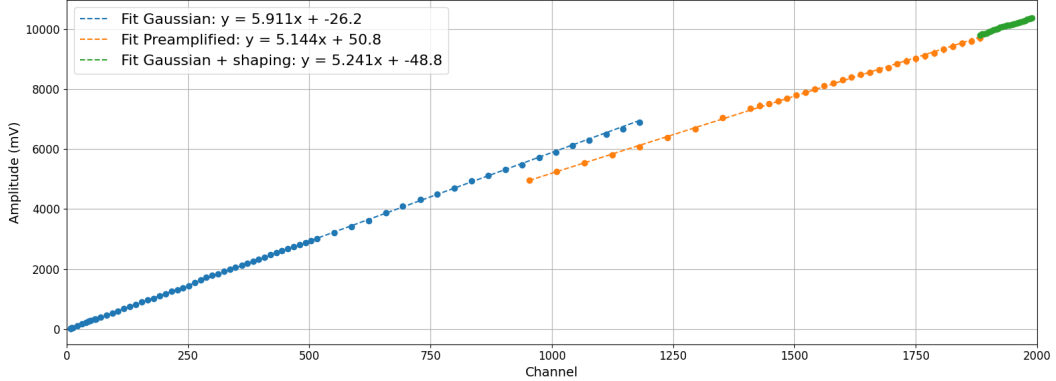


**Fig. 6:** ADC integral linearity

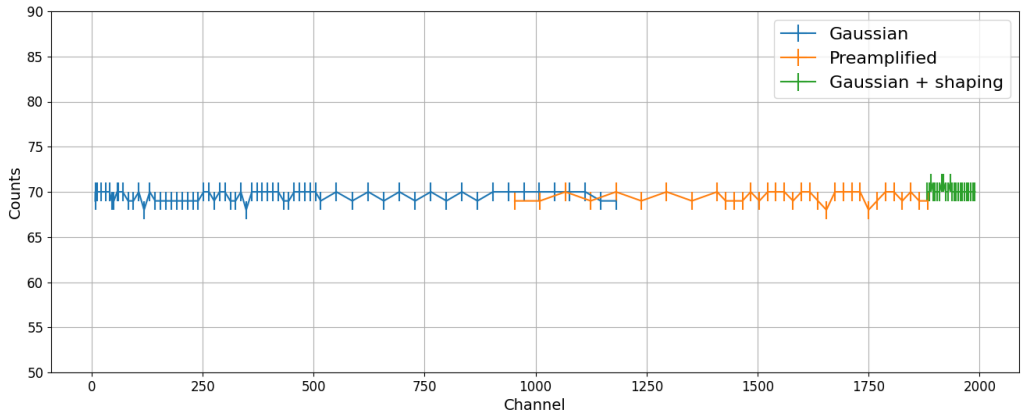


**Fig. 7:** ADC differential linearity

2 or at most 3 bins, probably due to voltage fluctuations. In these cases, it was chosen to assign an average bin, calculated as a weighted average of the counts in the bins involved.

### 2.5. Conclusions about linearity

The integral linearity measurements confirm that the ADC-MCA system behaves linearly within its optimal operating range, with expected deviations near the voltage extremes due to distortion or saturation effects. However, the differential linearity test shows a nearly flat response with approximately 70 counts per channel instead of the expected 250, indicating that a significant fraction of pulses are not being registered. This constant but reduced count level across channels suggests the presence of acquisition inefficiencies such as dead time, threshold effects, or signal processing limitations that reduce the effective counting rate. Despite this, the uniformity of the differential response within the central channels confirms stable and consistent ADC performance in that range. Overall, the system is linear

but requires further optimization to improve pulse detection efficiency and reach the expected counting rates.

To determine whether the count deficit was due to a malfunction of the ADC or of the pulser, we first calculated the spectrometer efficiency and the source activity. We then compared the actual count rate in the spectra used for the high-voltage-gain calibration with the count rate predicted from those parameters. A discrepancy of approximately 7% was observed, indicating that the loss of counts is primarily attributable to the pulser, which may malfunction at excessively low repetition frequencies.

## 3. Coincidence techniques and stability

### 3.1. Auto-coincidence

In this section of the experiment, the 1" detector was used and placed in front of the source. The output signal from the detector was sent to the AMP-TSCA, which was then analysed using an oscillo-

scope for both outputs (AMP and SCA). From the signal analysis, it was observed that a NIM [12] signal was produced subsequent to the reception of the maximum analog signal. In this configuration, auto-coincidence could not be detected. The MCA, indeed, required the logic signal to arrive before the maximum of the analog signal and extend for at least 500 ns after this [7]. To resolve this limitation, the output signal from the preamplifier was then split. One copy of the signal was sent to the AMP, which allowed the output signal to be delayed by  $2\ \mu s$ . The other copy was sent to the AMP-TSCA used to generate the logic signal.

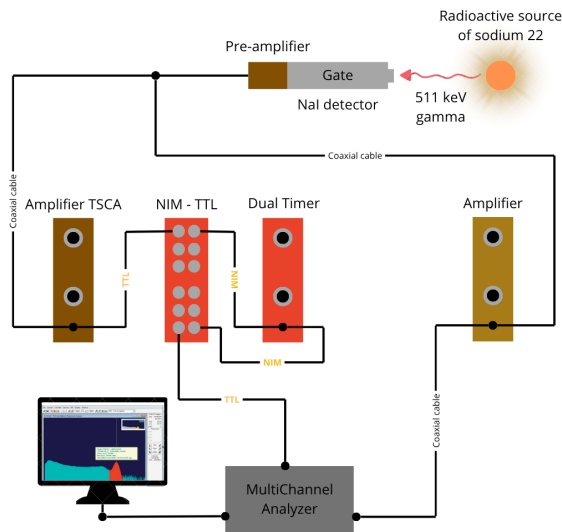


**Fig. 8:** Electronic chain for auto-coincidence.

In this new configuration, the logic signal arrived before the peak of the analog signal, but it still did not meet the requirement to extend temporally beyond it. To overcome this problem, a Dual Timer was used to temporally dilate the logic signal, thus enabling the detection of auto-coincidences.

To ensure proper communication between the AMP-TSCA and the Dual Timer, an additional module, the NIM-TTL-NIM, was used to convert the logic standards according to the operating specifications required by the various modules. The final chain for this section is shown in Fig. 8.

### 3.1.1. Auto-coincidence spectrum

At this stage of the experiment, the *lower level* and *window level* settings of the SCA were used to accurately select the energy range corresponding to the peak centred at 511 keV. Once this selection was made, the 1" detector was used exclusively as a gate, and its spectrum no longer needed to be displayed. The selected spectrum is available in Fig. 9.

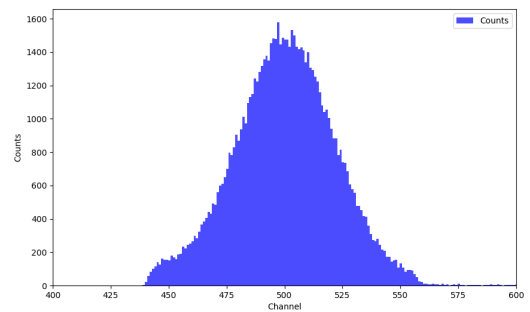


**Fig. 9:** Peak selected in auto-coincidence.

## 3.2. Coincidence

Coincidences follow the same logic as the electronic chain used for auto-coincidence, with the major difference that the signal was not split starting from a single scintillator, but was generated by two separate detectors. In this context, the 1" detector received the photon emitted at 511 keV back-to-back from the  $^{22}\text{Na}$  source and acted as a gate, while the 2" detector was used to observe the spectrum of the other photon as a function of the scattering angle. However, this configuration required a few edits. The signal from the gate, directed toward the AMP-TSCA, needed to be split and passed through a resistor placed in parallel with the module. This arrangement was used to emulate the voltage drop that was previously provided by the amplifier, thus reproducing the same conditions under which the energy window was selected. In the set-up used, a  $384\ \Omega$  resistor balanced the coincidence peak shift caused by this phenomenon.

Fig. 10 shows the electron chain exploited for the Compton experiment. This chain is the one used for coincidence, the only difference being that, between the source and spectrometer, a scatterer was interposed, the choice of which will be discussed in detail in Section 4.3.

### 3.2.1. Coincidence spectrum

At this point, a coincidence measurement was performed on the two back-to-back photons emitted by the  $^{22}\text{Na}$  source, resulting in the histogram shown in Fig. 11. The spectrum matches expectations, confirming the correct setup of the system. At this stage, the apparatus was ready to proceed with the Compton scattering experiment.

## 3.3. Stability

In order to observe how the gain and resolution of the apparatus varied and to study its response stability, just before the suspension of laboratory activities due to the Christmas vacations, it was decided

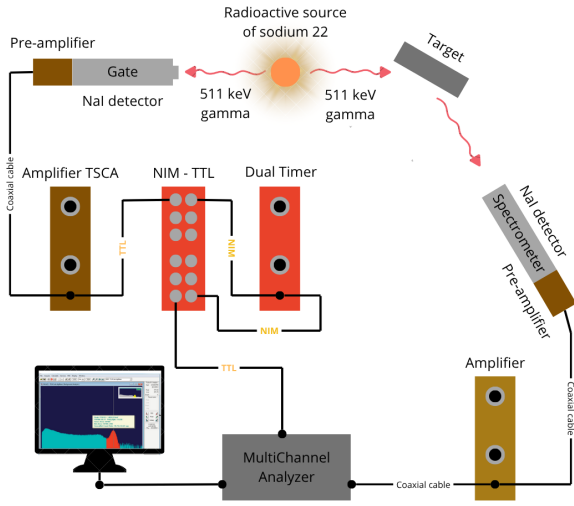


**Fig. 10:** Electronic chain for coincidence.

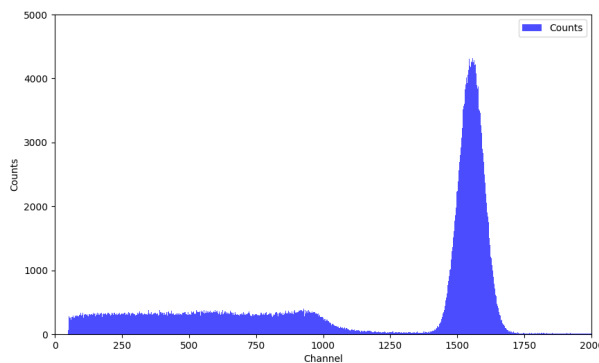


**Fig. 11:** Coincidence spectrum.

to turn off the power supplying the experimental setup and let the apparatus cool down, and then turn the power back on on Dec. 20, 2024. Thanks to a programmable "Job Control System", upon returning to the laboratory it was possible to make a plot showing the trend of the peak centroid at 511 keV and the energy resolution as a function of time. It was noted that with the passage of time the two quantities mentioned above exhibited an oscillatory and decreasing (but not damped) trend, making additional weeks of sampling necessary in order to be able to find a regime of stability that could be considered satisfactory.

These additional measurements made it possible to observe an almost linear trend as far as the energy resolution was concerned, a fit was made to determine the reference value that was then exploited for the subsequent sections, the graph is shown in Fig. 12.

In the case of the coincident peak centroid, a sat-

isfactory stability regime was not achieved. Therefore, similarly to the resolution, a linear fit was performed to extract a well-defined reference value for  $\mu$ . The corresponding results are presented in Fig. 13.

Slightly different values were obtained at the end of this period from those obtained before the shutdown with regard to the resolution and centroid value, since these parameters are crucial for subsequent analyses, it was decided to exploit the latter, the results are shown in Table 2.

	Resolution	Peak position
Coincidence	$(6.89 \pm 0.02)\%$	$1434 \pm 4$

**Table 2:** Final values for resolution and peak position in coincidence setup.

We then took this phenomenon into account in the discussion of errors in the corresponding Chapter 8.

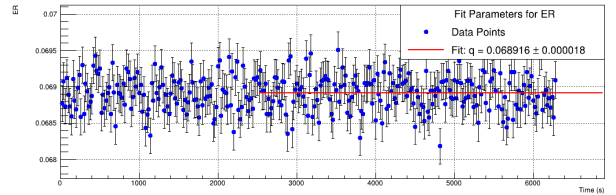


**Fig. 12:** Latest energy resolution trend.

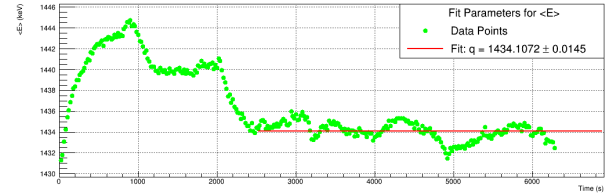


**Fig. 13:** Latest centroid position trend.

## 4. Experimental set up

### 4.1. Compton Scattering

Compton scattering is a physical phenomenon that describes the interaction between a photon (electromagnetic wave) and a charged particle, typically an electron. During this interaction, the photon transfers part of its energy to the electron, resulting in an increase in its wavelength (i.e. a decrease in its energy). The experimental test of this effect serves as a compelling evidence for the particle-like nature of electromagnetic radiation.

The Compton scattering formula was derived in detail in Appendix B.1. This relation connects the variation in the photon's wavelength ( $\Delta\lambda$ ) to the scattering angle  $\theta$  as follows:

$$\Delta\lambda = \lambda' - \lambda = \frac{h}{m_e c} (1 - \cos \theta). \quad (1)$$

The Compton cross-section describes the probability that a photon interacts with an electron via Compton scattering. At leading order, this value follows the Klein-Nishina formula:

$$\frac{d\sigma}{d\Omega} = \frac{r_e^2}{2} \left( \frac{E'}{E} \right)^2 \left[ \left( \frac{E'}{E} \right) + \left( \frac{E}{E'} \right) - \sin^2(\theta) \right] \quad (2)$$

To study all perturbative orders, semi-empirical formulas are used (analogous expressions were employed in the Monte Carlo simulation presented in Appendix C), which depend on the energy of the incident photon and the properties of the material, particularly the atomic number  $Z$  of the target. Since Compton scattering primarily involves electrons, its cross-section is proportional to the number of electrons per atom, which corresponds to  $Z$ .

In other words, materials with a higher atomic number  $Z$  exhibit a greater probability of Compton scattering, as they contain more electrons available for interaction.

In the energy range from X-rays to gamma rays, Compton scattering is one of the three main mechanisms by which radiation interacts with matter, alongside the photoelectric effect and pair production. The relative dominance of each phenomenon depends on the photon energy and the  $Z$  value. At higher energies, Compton scattering tends to dominate over the photoelectric effect, whereas pair production becomes significant only at even higher photon energies.

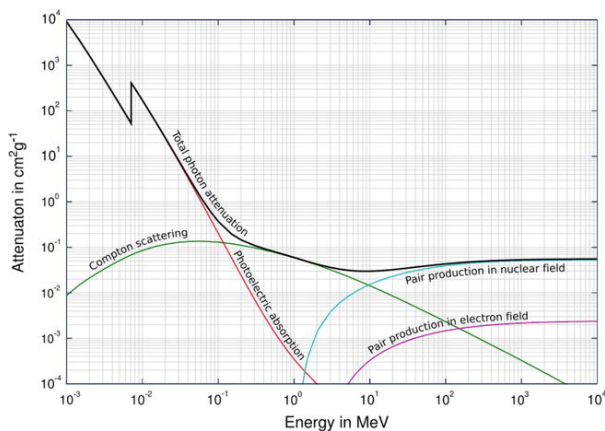
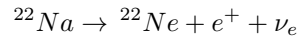


**Fig. 14:** Cross sections for Pb ( $Z = 82$ ) as a function of incident photon energy. [13]

In our experiment, a  $^{22}\text{Na}$  source was used. This isotope undergoes beta-plus ( $\beta^+$ ) decay, emitting a

positron ( $e^+$ ) and an electron neutrino ( $\nu_e$ ):



The decay (which has a half-life of 2.6 years) leads to  $^{22}\text{Ne}$  and is accompanied by the emission of a 1274 keV photon (BR = 90.4%). There is also a possibility of electron capture (9.5%), which brings the system to the same excited state of neon. The emitted positron is of particular interest, as it is an antimatter particle generated in a matter system and will rapidly annihilate, producing two back-to-back photons of 511 keV. One of these photons undergoes Compton scattering in the target, while the other is used to generate a coincidence gate, thereby reducing background noise.

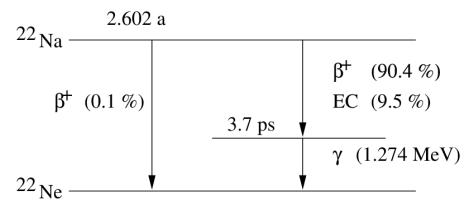


**Fig. 15:**  $^{22}\text{Na}$  decay scheme. [14]

## 4.2. Alignment

In order to avoid any problem with the alignment of the system, time was spent building supports out of Lego to make the whole structure more aligned (Fig. 16). We can say that the alignment is within a few millimetres, thanks also to the use of a caliper for greater precision.

The initial idea was to implement a servo motor in the structure to rotate the target with an Arduino program, but this was not implemented in the experiment as it was observed that the servo motor had an inaccuracy of the order of  $5^\circ$  instead of  $1^\circ$  as reported by the manufacturer. The manual approach was therefore opted for, in order to limit the sources of error.

The alignment of the setup was carried out using a laser as a reference tool. Initially, the target was removed and a laser was placed in its position. By turning on the laser, it was possible to rotate the target holder and adjust its inclination to the correct angle. Subsequently, the target was repositioned in its place, and the laser was mounted instead on the rotatable movable base located at the bottom of the apparatus. After selecting the desired angle, a perforated guide was positioned such that the laser beam could pass through the centre of the target holder. This allowed us to verify and fine-tune the alignment of the system. Finally, the spectrometer was mounted on the holder, properly aligned along the verified laser

path.

We also chose to raise the detectors above the work surface to decrease interference phenomena with the table.



**Fig. 16:** Lego supports.

### 4.3. Target material selection

The choice of target material depends on the trade-off between the probability of Compton scattering, which increases with the atomic number  $Z$ , and the reduction of competing effects, such as the photoelectric effect and absorption. Three metals were available in the laboratory:

- Aluminium ( $Z = 13$ ): With a lower atomic number, aluminium minimizes the photoelectric effect, which becomes less relevant at low  $Z$ . However, the probability of Compton scattering is lower compared to materials with higher  $Z$ , reducing the intensity of the measurable signal.
- Copper ( $Z = 29$ ): This is a balanced choice. Its intermediate  $Z$  ensures a good probability of Compton scattering without the photoelectric effect becoming too dominant. Moreover, copper has a density and mechanical strength that make it practical and lightweight.
- Lead ( $Z = 82$ ): Although lead has a high probability of Compton scattering due to its high  $Z$ , it also enhances competing phenomena, such as the photoelectric effect ( $\sim Z^5$ ), which may interfere with the measurement. Furthermore, the high absorption of incident photons can reduce the number of observable useful events.

Based on these considerations and on some Monte Carlo simulations (Fig. 17) carried out by us, we concluded that copper is the optimal scattering material for our experiment.

### 4.4. Thickness

The thickness of the target was as well a parameter that needed to be carefully evaluated; two possible configurations were considered for the experiment.

- **Transmission:** photons emitted by the source pass through the target before reaching the detector.
- **Reflection:** incident photons pass through a portion of the material and are then scattered backward toward the spectrometer.

In both cases, the probability that a photon reaches a depth  $x$ , undergoes Compton scattering, and then exits in a direction  $\theta$  without any further interactions was considered.

The product of the probabilities along both paths is integrated over all possible interaction depths  $x$ , and then, in order to find the optimum for this function, it is differentiated with respect to the thickness  $D$ .

In the reflection geometry, the calculation is carried out with a specific inclination of the target, chosen to simplify the problem: the normal to the target lies along the bisector of the desired scattering angle as shown in Fig. 19. In the transmission framework, instead, the target was fixed at  $0^\circ$  (contrary to the suggestion in Zanotti's paper [15], visible in Fig. 18). The main reason for this choice was the outcome of GeoGebra simulations (Fig. 21), which showed that this configuration slightly improves the energy resolution, at the cost of a lower count rate for higher angles; in addition, it helped to avoid accumulating errors due to target inclination. A diagram of the configuration is available in Fig. 23.

From the final solutions, isolating  $D$ , the following trends are obtained:

- Transmission:  $D = \lambda_T \ln\left(\frac{\lambda_T + \lambda' \cos(\theta)}{\lambda_T}\right)$
- Reflection:  $D \rightarrow \infty$

In these expressions,  $\lambda$  and  $\lambda'$  represent the photon attenuation coefficients in the medium, corresponding respectively to the incident energy (511 keV) and to the energy after scattering. These values are tabulated by NIST.<sup>1</sup>

The factor :

$$\frac{1}{\lambda_T} = \frac{1}{\lambda} - \frac{1}{\lambda' \cos(\theta)}$$

represents a composite factor of the two mentioned before, where  $\theta$  represent the scattering angle.

The infinite thickness value in the reflection case is, of course, only a theoretical limit. However, considering that the interaction probability follows the

<sup>1</sup><https://physics.nist.gov/PhysRefData>

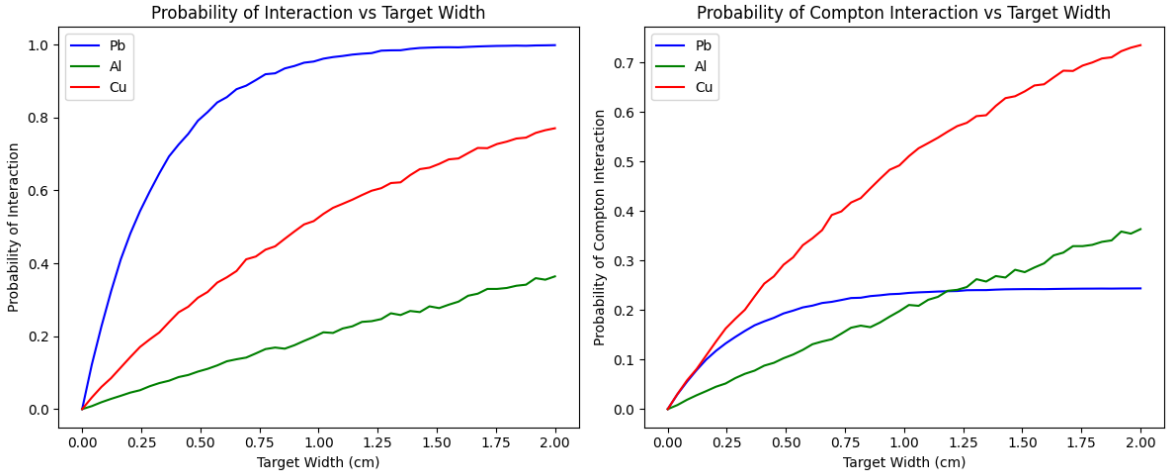


**Fig. 17:** Interaction probability as a function of target depth for Lead (Pb), Copper (Cu) and Aluminium (Al); for both Compton scattering and photoelectric effect on the left and for only Compton scattering on the right.

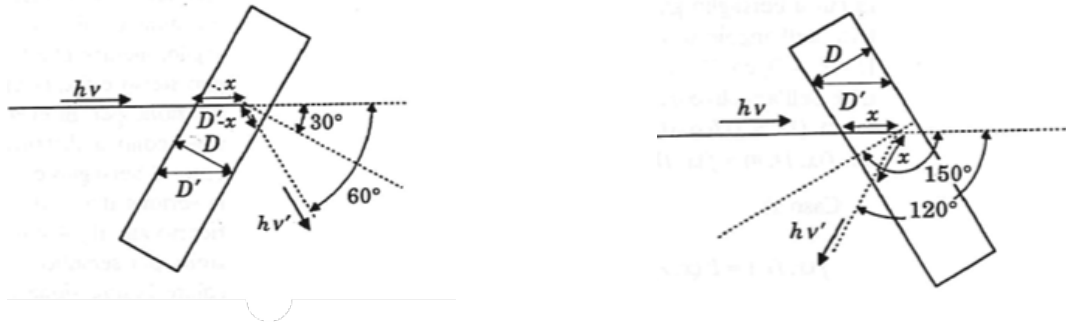


**Fig. 18:** Geometrical study of Compton scattering in transmission. [15]

**Fig. 19:** Geometrical study of Compton scattering in reflection. [15]

exponential law  $P(x, \lambda) = e^{-x/\lambda}$ , once a thickness is chosen it becomes straightforward to estimate the fraction of the beam that passes through the material without interacting.

In Fig. 20, the trend of the optimal target width as a function of the scattering angle is shown. It can be observed that a thickness of 1 cm represents a good compromise among all the available target widths in our laboratory. In a real experimental context, obtaining a target with infinite thickness is not feasible; therefore, a balance had to be found between theoretical predictions and practical constraints. The choice of a 1cm thick target aligns well with theoretical expectations for the transmission configuration, while also ensuring ease of handling and avoiding the need for significant modifications to the experimental setup before each measurement.

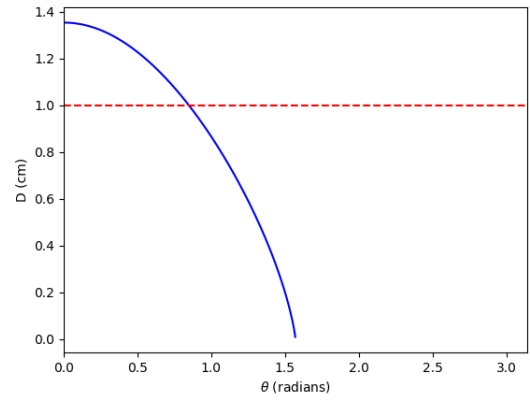


**Fig. 20:**  $D$  value in transmission as a function of the scattering angle,  $\theta$ . The red dashed line represent the chosen thickness of 1 cm.

The full details of the above calculations are reported in the Zanotti article [15], but are also available in Appendix E.

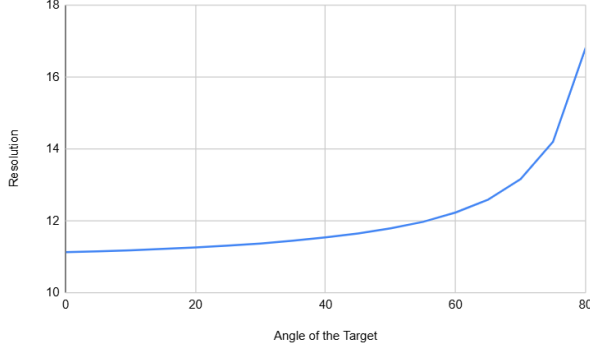


**Fig. 21:** Resolution values as a function of the target angle in the transmission setup at the fixed spectrometer angle of  $45^\circ$ .

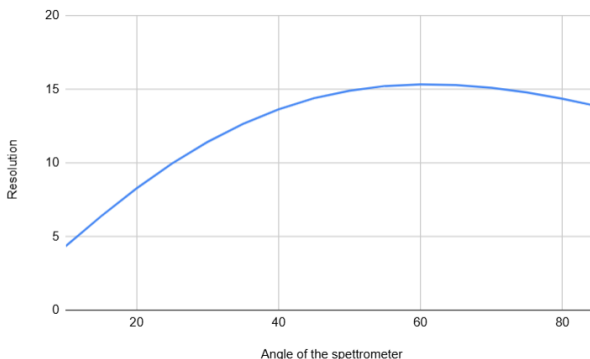


**Fig. 22:** Resolution values as a function of the spectrometer angle in the transmission setup at the fixed target angle of  $0^\circ$ . Thanks to this simulation we decided to take only small angle in the transmission configuration.

#### 4.5. Distances

It is also necessary to investigate the optimal distances for placing the detectors, the target, and the source in order to remain within the energy resolution limits of our detectors and avoid dead-time.

##### 4.5.1. Spectrometer-target distance

To determine the optimal distance between the detector and the target, it is necessary to derive the Compton formula (Eq. 1) in order to obtain a relationship between the energy variation  $dE'$  and the angular variation  $d\theta$ :

$$dE' = \frac{E' \cdot \sin(\theta)}{2 - \cos(\theta)} d\theta$$

The minimum of this function occurs at an angle  $\theta_{\min} = \sqrt{3}$  rad. The product of  $\theta_{\min}$  and the angular resolution gives the width of the unresolved energy cone, which we denote as  $\theta^*$ .

If we consider a detector with diameter  $d$ , the distance  $l$  required for the angle  $\theta^*$  to match the angular aperture of the resolution cone is given by:

$$l = \frac{d/2}{\tan(\frac{\theta^*}{2})} \quad (3)$$

Using the experimental parameters for energy resolution and the detector diameter, Eq. 3 yields an optimal value of approximately 43 cm. However, the simulation carried out with GeoGebra shows that at this distance the resolution of our setup would be ineffective: the difference between the photon energy incident on the detector in the cases of minimum and maximum energy would be too large to allow for an accurate measurement. This discrepancy can be explained by considering that Eq. 3 assumes a collimated beam, whereas in reality we have an angular aperture of the cone that introduces unaccounted effects.

To obtain an energy cone compatible with the detector's resolution, it would be necessary to place the detector at a distance of about 97 cm. However, this was not possible for two reasons:

- **Spatial limitations:** the experimental setup does not allow the detector to be placed at such a distance.
- **Decrease in count rate:** increasing the distance would significantly reduce the photon flux detected, making data acquisition impractical within a reasonable time frame.

Therefore, the detector was ultimately positioned at a distance of 25 cm from the target, representing a compromise between energy resolution and acquisition efficiency. Although this placement resulted in an angular aperture that exceeds the ideal resolution cone, it ensured a sufficient count rate for practical data collection.

##### 4.5.2. Gate-source distance

Using Eq. 3 again with the parameters related to the gate detector, we find that the optimal positioning distance is 16 cm.

In the GeoGebra simulations, the escape depth of a 511 keV photon in a sodium iodide scintillator crystal was also considered. The interaction depth was chosen to correspond to the thickness of the gate detector (equal to 1"), since this is the component that triggers the detection.

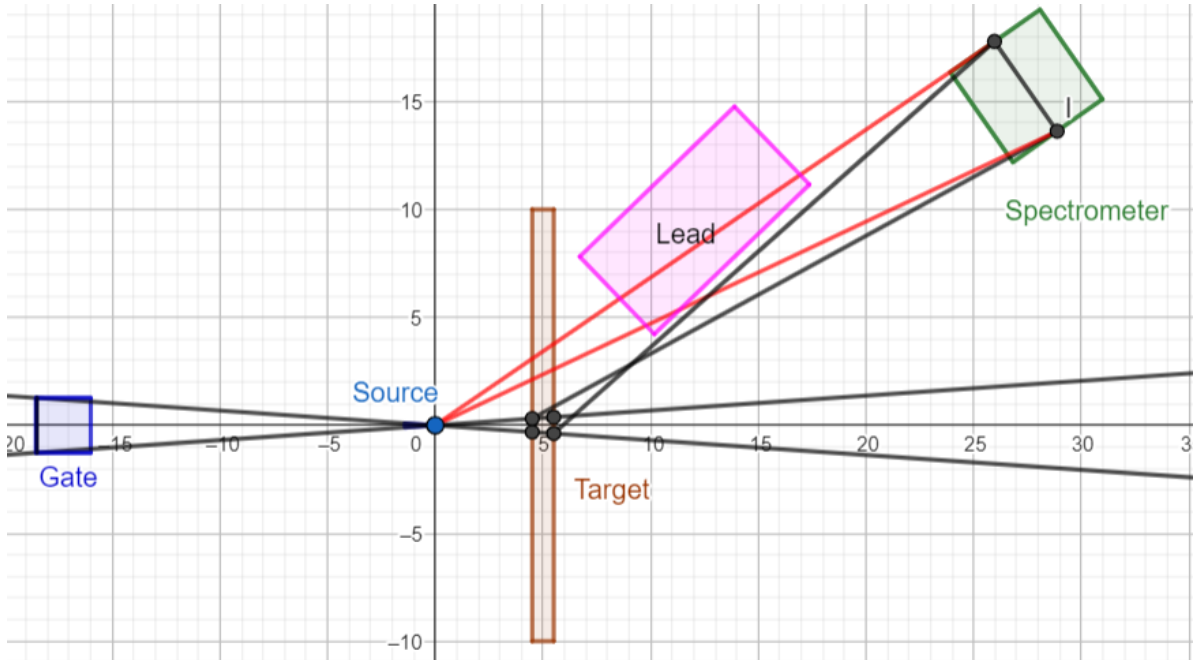


**Fig. 23:** GeoGebra simulation of the transmission geometry.

#### 4.5.3. Source-target distance

The best condition occurred when the target was in contact with the source, since this resulted in a more collimated interaction cone. However, in order to maintain the ability to rotate the target, it was necessary to leave a gap of approximately 4.5 cm from the source to the centre of the target.

#### 4.6. Activity

To measure the activity of the source, an equation that relates the number of counts  $N_c$  to the activity of the source at time  $t$ ,  $S(t)$ , through the intrinsic peak efficiency  $\epsilon$ , the measurement time  $t_{mis}$  and the solid angle subtended between the source and the detector  $\Delta\Omega$  was used:

$$N_c = S(t) \cdot \epsilon \cdot \frac{\Delta\Omega}{4\pi} \cdot t_{mis} \cdot BR \quad (4)$$

To use this equation, it is necessary to verify, using a calibrated source, that the efficiency of our NaI(Tl) detector is consistent with the tabulated value within the experimental uncertainty.

In the laboratory we have a  $^{60}\text{Co}$  source with a certified activity as of 01/10/2014 of  $S_0 = 393 \text{ kBq}$ .

$^{60}\text{Co}$  emits two photons per decay, according to the scheme shown in Fig. 24.

Considering the initial activity  $S_0$  and the half-life of the source ( $t_{1/2} = 1925$  days), the following relation holds:

$$S(t) = S_0 \cdot \left(\frac{1}{2}\right)^{T/t_{1/2}} \quad (5)$$

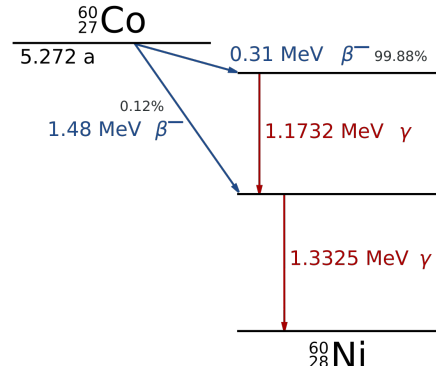


**Fig. 24:**  $^{60}\text{Co}$  decay scheme. [16]

Where  $T$  represents the time elapsed (in days) between the certification date of the source and the day of the measurement, equal to 3759 days. With this consideration, it was possible to determine the activity at the measurement date, which was  $S(15/01/2025) = 101544 \text{ Bq}$ . Given the long decay time of the source, the activity was assumed constant during the data acquisition period.

Placing the source at 15 cm from the 2" detector and aligning it along the axis, the solid angle subtended can be calculated using:

$$\frac{\Delta\Omega}{4\pi} = \frac{1 - \cos(\theta^*)}{2} \quad (6)$$

$$\theta^* = \arctan\left(\frac{2,54}{15}\right)$$

$$\frac{\Delta\Omega}{4\pi} = (7, 25 \pm 0, 23) \times 10^{-3}$$

The source was therefore placed in front of the detector, and the measurement was carried out for 20 minutes ( $= 1200$  seconds), after which the spectrum was analysed, as shown in Fig. 25.

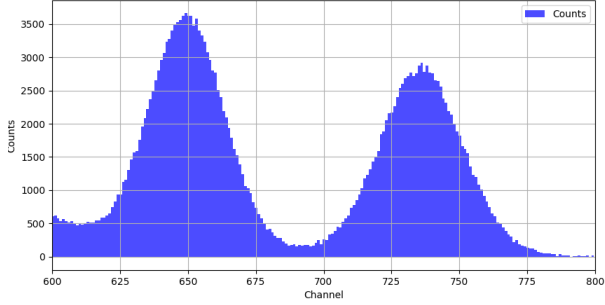


**Fig. 25:** Cobalt doublet.

It was then possible to determine the number of counts under the peaks; from these, the efficiency was obtained by appropriately inverting Eq. 4. For a cleaner measurement, a background spectrum with the same live time characteristics was subtracted from each spectrum.

**Table 3:** Obtained efficiency values.

E (keV)	$\epsilon_{exp}$ (%)	$\epsilon_{table}$ (%)	Comp.
1173	$13,33 \pm 1,12$	$12,72 \pm 0,63$	64%
1332	$12,28 \pm 1,03$	$11,66 \pm 0,58$	60%

Since the  $\gamma$  de-excitation cascade of cobalt occurs on a timescale characteristic of electromagnetic interactions, it may happen that our detector recorded some events within the sum peak. For this reason, it was necessary to correct the number of photons actually detected.

Assuming, as a first approximation, an isotropic emission of the two photons, the probability that both reach the detector is simply the square of the subtended solid angle. Taking into account the probability that the photons undergo photoelectric absorption in the crystal, we obtained a correction of 0.015%.

Having verified the compatibility between the experimental values and the tabulated ones, we used the values provided in the ORTEC data sheet [17] for the peak efficiency of the 1274 keV and 511 keV photons typical of  $^{22}\text{Na}$ .

We then used Eq. 4, appropriately inverted, to calculate the activity  $S(t)$ , where the number of counts

was obtained from the spectrum analysis after background subtraction:

$$\text{Activity (Bq)} = (188900 \pm 11647) \text{ Bq}$$

This value is fully compatible (distance of  $0.255\sigma$ ) with the activity declared by the manufacturer at the measurement date, which is  $(179149 \pm 35829)$  Bq.

#### 4.7. Efficiency

In the Ortec datasheet [17], a plot of the efficiencies for three sodium iodide detectors (1.5", 2", and 3", respectively) was provided. The data were extracted from these curves, and a fit was performed to estimate intermediate values. This interpolation (Fig. 26) was not based on a specific model, but solely aimed at providing a reliable prediction of intermediate values between the given data.

Noting that the efficiencies were evaluated at the same photon energy, we performed a linear regression of the efficiencies at that fixed energy as a function of the detector diameter. In this way, we extracted the corresponding value for a 1" detector. A further fit was then performed using the same functional form, in order to obtain a prediction of the efficiency values of interest.

$$\epsilon_{gate}(511) = (14.70 \pm 1.67)\%$$

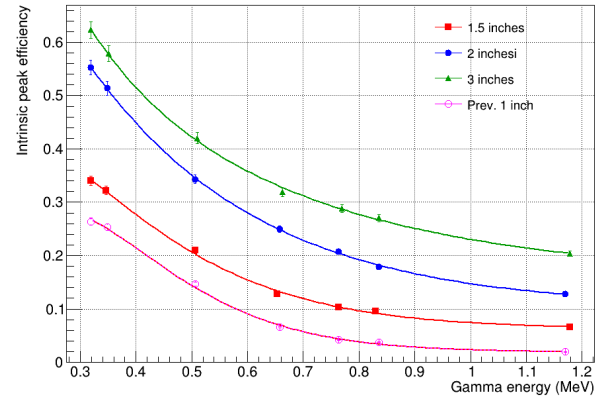


**Fig. 26:** Interpolation of efficiency data extracted from the ORTEC [17] datasheet.

#### 4.8. Calibration

In order to perform energy measurements, calibrating the apparatus is essential.

With this purpose in mind, we placed several available laboratory sources in front of the spectrometer, acquired the spectrum of each, and subtracted an appropriate environmental background. The detected peaks are available in Table 4 .

**Table 4:** Peaks used for energy calibration

Source	E (keV)	Channel
$^{210}\text{Pb}$	46,5	$155,88 \pm 7,97$
$^{241}\text{Am}$	59,54	$197,64 \pm 6,23$
$^{44}\text{Ti}$	67,86	$222,54 \pm 5,49$
$^{44}\text{Ti}$	78,32	$254,41 \pm 5,58$
$^{57}\text{Co}$	122,06	$375,30 \pm 6,47$
$^{44}\text{Ti}$	146,92	$451,18 \pm 9,11$
$^{226}\text{Ra}$	186,21	$556,83 \pm 11,81$
$^{210}\text{Pb}$	241,9	$706,88 \pm 11,34$
$^{210}\text{Pb}$	295,1	$856,78 \pm 10,55$
$^{210}\text{Pb}$	351,9	$1016,62 \pm 10,30$
$^{44}\text{Ti}$	511	$1467,69 \pm 8,88$
$^{214}\text{Bi}$	609,3	$1736,65 \pm 16,86$
$^{137}\text{Cs}$	661,65	$1879,85 \pm 27,17$

From this, a linear energy calibration can be obtained, as shown in Fig. 27. Thanks to this relation, it is possible to establish a correspondence between energy and channel number.

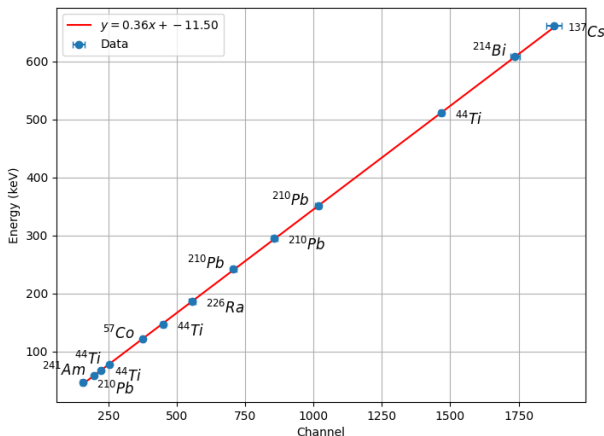


**Fig. 27:** Linear calibration of the apparatus.

## 5. Measurements

We now dedicate this section to the study and analysis of the measurements performed in both configurations.

### 5.1. Shielding

Before proceeding with each measurement, we carefully shielded the direct line of sight between the source and the spectrometer using lead blocks. This choice was motivated by the desire to minimize the presence of the 511 keV peak (due to annihilation) and its associated Compton continuum, in order to lower the background level onto which the peak of interest would be superimposed.

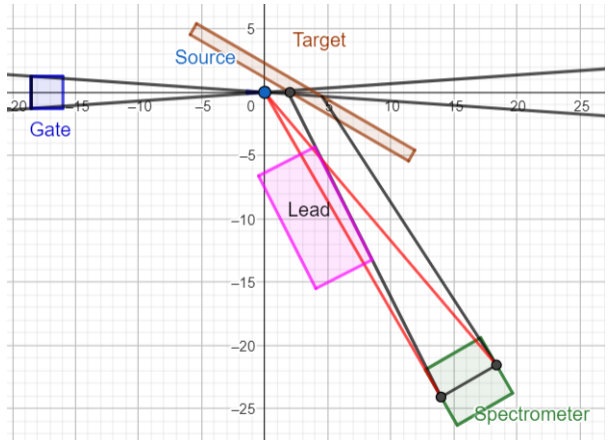


**Fig. 28:** Shielding geometry with Pb blocks from GeoGebra simulation.

As illustrated in Fig. 28, we made use of a geometric simulation performed with GeoGebra, setting up a reference system centred on the source, in order to optimally position the lead blocks. This made it possible to effectively shield unwanted radiation without obstructing the beam useful for measurement.

Otherwise, we chose not to shield the area around the spectrometer. The use of lead in the vicinity of the detector would in fact have introduced an additional peak, due to the X-fluorescence of the lead itself, typically observable at around 75 keV, which could overlap or interfere with the signals of interest. While we are aware that the absence of shielding around the spectrometer may increase the number of random coincidences, we considered this side effect more manageable than the contamination introduced by the lead peak.

### 5.2. Energy spectra analysis

The energy spectra were acquired as histograms with a binning chosen such that each bin used in the fit contained at least 80–100 events. When this condition was not naturally met, a re-binning procedure was applied. This ensured that the statistical distribution in each bin could be well approximated by a Gaussian distribution.

In order to analyse the spectra and, in particular, to accurately measure the number of counts per peak, it was crucial to effectively separate the background from the peak signal. Since the spectra presented complex shapes for which no analytical expression exists, the background was preliminarily fitted with a polynomial function of the form:

$$h(x) = ax + bx^2 + cx^3 + dx^4$$

where  $x$  represents the energy in channels, as the energy calibration was applied only after this step.

For small angles (below  $50^\circ$ ), where the 511 keV annihilation peak overlaps with the peak of interest, a Gaussian term centred at  $E = 511$  keV was added to the background function  $h(x)$ .

The use of a fourth-degree polynomial is justified by the fact that any sufficiently smooth analytical function can be approximated by a Taylor series. Thus, truncating the expansion at the fourth order provides a flexible yet controlled approximation over the domain.

To analyse the photopeaks, a Gaussian component was added to the fitting function to model the peak. After performing the fit, the integral of the background function was subtracted from the integral of the total fit function. Since the two functions differ only in the peak region, this method provides a reliable estimate of the net signal counts.

Examples of these preliminary analyses can be seen in Figures 29 and 30.

The full analysis, including all spectra and fit details, is available in the associated GitHub repository.

### 5.3. Transmission measurements

In the transmission configuration (Fig. 18) we opted to leave the target fixed at  $0^\circ$ , this choice (from GeoGebra simulation) yields better resolution as previously explained in Section 4.4.

From the spectrum analysis, the parameters visible in Table 5 were collected.

A smaller angle of  $15^\circ$  was also taken; in this configuration the centroid of the Compton peak fell within the FWHM of the 511 keV annihilation peak. The peak could not be resolved, and we could only make an estimate of the centroid, without gaining any information about the rate that characterised the measurement.

### 5.4. Reflection measurements

As in the previous case, we collected several measurements by sweeping a set of major angles. The results of the collection can be seen in the Table 6. In particular, we point out the difficulty in evaluating the angle of  $40^\circ$ , which has a much lower rate than one would expect for that value and is totally incompatible with Klein-Nishina. We have taken this data several times by making 4 data collections at different times and with different methods (reflection and transmission). The 4 rate values were compatible with each other, but as already mentioned, not compatible with the remaining trend. Unfortunately, we were not able to find a comprehensive answer for this particular problem, so we reserve the right to treat it as an outlier and carry out our analysis by discarding it.

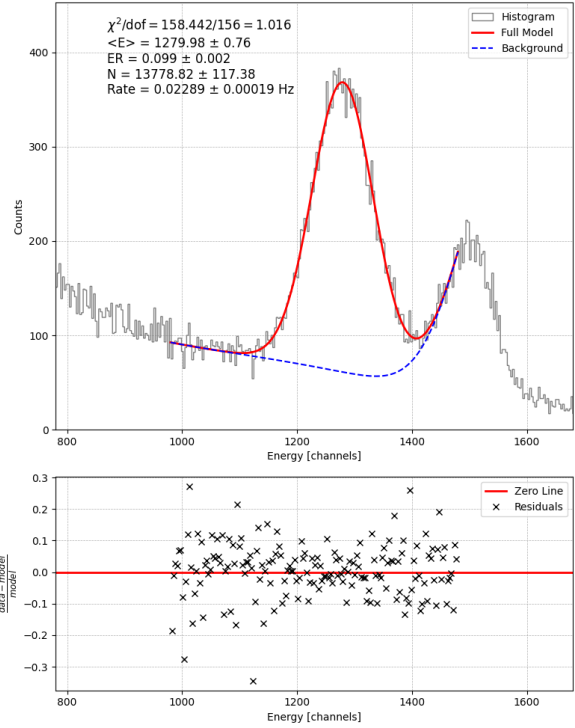


**Fig. 29:**  $35^\circ$  Compton peak fit.

## 6. Cross Section Data Analysis

It is now possible to write:

$$\frac{N}{T \cdot \Omega_{spect}} = \phi_{gate} \cdot \epsilon_{spect}(\theta) \cdot n_c \cdot \wp(\theta; \lambda, \lambda') \cdot \frac{d\sigma}{d\Omega} \quad (7)$$

where  $\phi_{gate}$  is the number of photons that open the gate each second,  $n_c$  is the density of scattering centres,  $\wp(\theta; \lambda, \lambda')$  represent the probability, even if it is not a real probability factor in a mathematical sense, for a photon to undergo just a single Compton scattering and be emitted on the right angle and  $\epsilon_{spect}(\theta)$  is the spectrometer efficiency as a function of the gamma energy. On the other side there is  $T$  that is the time measurement,  $N$  that represent the counts in the Compton peak and  $\Omega_{spect}$  is the solid angle subtended by the spectrometer.

Each of these parameters needs to be calculated precisely in order to assess the compatibility with the Klein–Nishina formula.

### 6.1. Density of scattering centre

To a first approximation,  $n_c$  is the number of electrons in the target per  $\text{cm}^3$ , this parameter can be computed using the following:

$$n_c = \rho \frac{N_a Z}{MM}$$

**Table 5:** Experimental measurements at different transmission angles.

Angle (°)	Rate (cps)	Counts	Channel	Sigma
35	$0.0229 \pm 0.0002$	$13778.8 \pm 117.4$	$1279.98 \pm 0.76$	$53.70 \pm 0.98$
40	$0.0199 \pm 0.0002$	$7697.7 \pm 87.7$	$1258.76 \pm 0.90$	$56.69 \pm 1.00$
50	$0.0142 \pm 0.0001$	$10812.7 \pm 104.0$	$1131.67 \pm 0.77$	$55.72 \pm 1.01$
60	$0.0107 \pm 0.0001$	$5953.8 \pm 77.2$	$1024.84 \pm 1.22$	$54.75 \pm 1.46$

**Table 6:** Experimental measurements at different reflection angles.

Angle (°)	Rate (cps)	Counts	Channel	Sigma
40	$0.0174 \pm 0.0001$	$17217.2 \pm 131.2$	$1205.01 \pm 0.58$	$55.59 \pm 0.60$
50	$0.0435 \pm 0.0004$	$12966.1 \pm 113.9$	$1107.01 \pm 0.66$	$59.94 \pm 0.61$
60	$0.0363 \pm 0.0004$	$10859.8 \pm 104.2$	$1008.55 \pm 0.86$	$56.04 \pm 1.08$
70	$0.0248 \pm 0.0002$	$17053.5 \pm 130.6$	$912.27 \pm 0.52$	$47.22 \pm 0.52$
80	$0.0205 \pm 0.0001$	$20263.8 \pm 142.4$	$828.23 \pm 0.45$	$41.96 \pm 0.45$
90	$0.0149 \pm 0.0001$	$14779.3 \pm 121.6$	$767.43 \pm 0.52$	$37.88 \pm 0.55$
100	$0.0130 \pm 0.0001$	$9535.5 \pm 97.6$	$698.66 \pm 0.61$	$35.01 \pm 0.62$
110	$0.0148 \pm 0.0002$	$9320.2 \pm 96.5$	$656.88 \pm 0.51$	$27.50 \pm 0.50$

where:

- $\rho$  is the density of the scattering target,
- $N_a$  is Avogadro's number,
- MM is the molar mass of the scattering target,
- $Z$  is the atomic number.

By substituting the corresponding known values for copper, one obtains:

$$n_c = 2.46 \times 10^{24} \frac{\text{electrons}}{\text{cm}^3}$$

The number will be considered exact, i.e., without errors due to the high precision with which all the aforementioned quantities are known.

## 6.2. Number of photons opening the gate

We can think at the number of photons per second that open the gate as:

$$\phi_{gate} = 2 \cdot S(t) \cdot BR \cdot \frac{\Delta\Omega_{gate}}{4\pi} \cdot \epsilon_{gate} \quad (511)$$

where:

- $S(t)$  is the source activity in Bq,
- BR is the branching ratio of the 511 keV photon,
- $\frac{\Delta\Omega_{gate}}{4\pi}$  is the solid angle covered by the detector,
- $\epsilon_{gate}(511)$  is the gate detector efficiency for the 511 keV photon,

- And the 2 represents the back to back emission of two photons.

Each of these quantities have already been calculated in the previous sections, or is considered known, such as the time and the branching ratio (BR). Only the solid angle deserves some further discussion; it follows Eq. 6, using a distance of 16 cm and a radius of 0.5" (half the diameter of the detector acting as the gate).

$$\frac{\Delta\Omega_{gate}}{4\pi} = (1.17 \pm 0.05) \times 10^{-3}$$

As already explained in the previous sections (see Section 4.5.2), a 1" escape depth was added to the distances to account for the photon interaction probability.

From this analysis, it emerges that the gate is opened at a frequency of:

$$\phi_{gate} = 58.6 \pm 8.2 \text{ Hz}$$

From the beginning of the experiment, particular attention was paid to avoiding pile-up phenomena during the measurements. To this end, the dead time of the system was continuously monitored to ensure it remained below the threshold of 5% of the total data acquisition time. This guaranteed the correct processing of pulses by the electronic chain, preventing, in most cases, the overlapping of signals, thereby improving both the efficiency and the precision of the measurements.

To achieve this, the gate detector was placed at a sufficiently large distance so that the detection cone narrowed, effectively reducing the rate of photons interacting with the detector crystal.

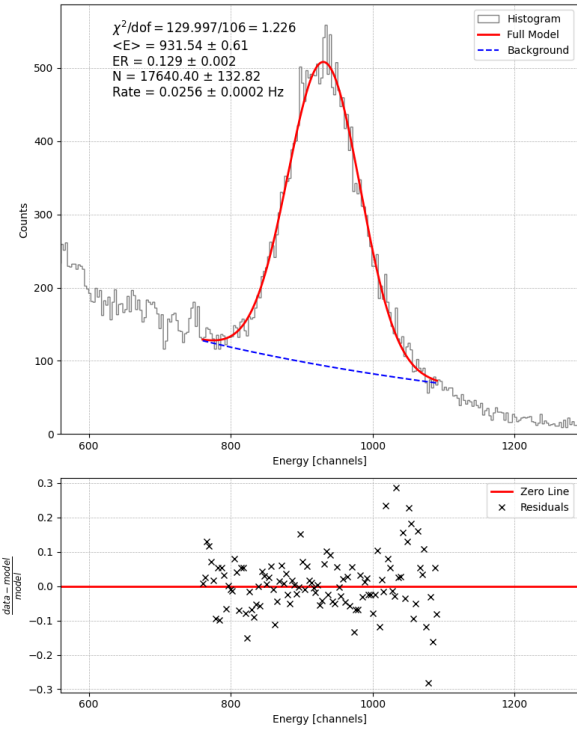


**Fig. 30:** 70° Compton peak fit.

### 6.3. Probability factor

This factor, whose explicit computation is presented in Appendix D, strongly depends on the geometry of the setup.

It is obtained by integrating the probability that a photon that undergoes a Compton interaction at depth  $x$ , is scattered at an angle  $\theta$ , and then does not interact again along the remaining path within the target.

The calculation procedure mirrors the one used in the determination of the optimal thickness in Section 4.4 (refer to the figures there for a clearer visualization), with the only difference being that the final derivative with respect to  $D$  is not performed here.

The resulting factor (which we refer to as the probability factor) is not dimensionless, but has the dimensions of a length.

In the following, we report the results obtained for the two studied configurations.

For the reflection framework, we can write:

$$\wp(\theta; \lambda, \lambda') = \lambda_R \left( 1 - e^{-\frac{D'}{\lambda_R}} \right)$$

where:

- $D' = \frac{D}{\cos(\frac{\pi-\theta}{2})}$  and  $D$  is the target width,
- $\lambda$  is the mean free path for a 511 keV photon,

- $\lambda'$  is the mean free path for the photon after the scattering,
- $\frac{1}{\lambda'_R} = \frac{1}{\lambda} + \frac{1}{\lambda'}$  it's a composition of previous factors.

For the transmission geometry we can define:

$$\frac{1}{\lambda_T} = \frac{1}{\lambda} - \frac{1}{\lambda' \cos \theta}$$

and then the result becomes:

$$\wp(\theta; \lambda, \lambda') = \lambda_T \cdot e^{-D/(\lambda' \cos \theta)} \cdot \left( 1 - e^{-D/\lambda_T} \right)$$

In this section, we acknowledge a limitation of our model: it assumes a perfectly collimated initial photon beam, which is unrealistic in our experiment, where the isotropic source emits in all directions, resulting in a cone of relevant photons.

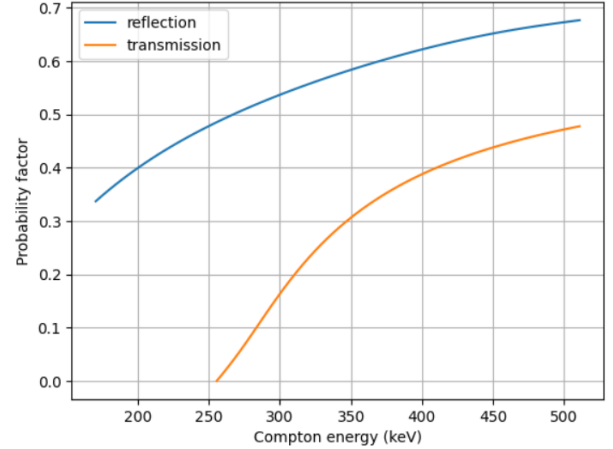


**Fig. 31:** Values of the probability factor in both reflection and transmission cases as a function of the scattered photon energy.

### 6.4. Spectrometer efficiency

For the spectrometer efficiency, we referred to the curve obtained in Section 4.7, specifically in Fig. 26, extrapolating the values for a 2" detector.

For the gate detector, the curve from the same figure for 1" detectors was used, evaluated at 511 keV.

### 6.5. Detection solid angle

As shown in Eq. 7, the study of the Compton scattering cross-section requires measuring the count rate per unit time and solid angle  $\Omega$ , that is the angle between the photon interaction point and the spectrometer.

Since the interaction point can vary for each photon, a Monte Carlo simulation described in Section C

was used to determine the probability distributions associated with the solid angles. To compute the solid angle, the interaction point for each photon was computed, and then the theorem of cosines [18] was used to determine the angle  $\beta$ :

$$(2R_{det})^2 = d_{IP-1}^2 + d_{IP-2}^2 - 2d_{IP-1}d_{IP-2} \cos(\beta)$$

where  $R_{det}$  is the detector radius and  $d_{IP-1}, d_{IP-2}$  are the distances from the interaction point to two diametrically opposite points on the detector circumference.

Once  $\beta$  is obtained, it is used to calculate the corresponding solid angle:

$$\Omega = \int_0^{2\pi} d\phi \int_0^\beta d\theta \sin(\theta) = 2\pi(1 - \cos(\beta))$$

Since  $\beta$  varies depending on the choice of points 1 and 2, we decided to consider two limiting cases and take their average: the case in which the two points lie on the horizontal ( $x, y$ ) plane, and the case in which they lie on the vertical plane perpendicular to it.

As the interaction point within the target varies, the angle obtained from the simulation also changes accordingly. A different *probability density function* (*PDF*) for each angle is obtained, as shown in Fig. 33.

We chose to use the median as the central estimate for the subtended solid angle, and to associate an uncertainty derived from the interquartile range (IQR), a suitable estimator for non-symmetric probability distributions due to its robustness with respect to outliers.

The results of this simulation are shown in Table 7 and 8.

## 7. Results

In this section, the main results obtained from the experimental data analysis are presented. Two key physical quantities are investigated: the electron mass, through the study of the energy of the scattered photons, and the classical electron radius, by analyzing the scattering rates.

Each quantity has been estimated by applying fitting procedures to different subsets of the data: reflection only, transmission only, and the combined dataset. The consistency of the results with theoretical expectations is also evaluated and discussed.

### 7.1. Measurement of the Electron Mass

To obtain an estimate of the electron mass,  $m$ , the energy of the scattered photons as a function of the scattering angle is studied; more details are pre-

sented in Appendix B.1.

$$E' = \frac{E}{1 + \frac{E}{mc^2}(1 - \cos \theta)} \quad (8)$$

By fitting the centroid of the Compton peak with the electron mass as a free parameter, an estimate can be obtained.

The results of these analyses are shown in Fig. 34. Looking at the results presented in Fig. 35, it can be seen that all the measurements are compatible within  $2\sigma$  with the expected value, and that the most precise measurement is the one performed in reflection.

### 7.2. Measurements of the Classical Electron Radius

By studying the rates, it is possible to obtain measurements of the cross-section and, consequently, of the Klein-Nishina formula, thanks to Eq. 7.

Further details on these equations are provided in Appendix B.2 and D.

Since the spectrometer efficiency and the factor  $\wp(\theta; \lambda, \lambda')$  vary as a function of  $\theta$ , for simplicity, the following ratio is considered:

$$\frac{N}{T} \frac{1}{\Omega_{spect} \cdot \epsilon_{spect} \cdot \wp(\theta; \lambda, \lambda')}$$

So that the two measurement (reflection and transmission) are now independent and can be used for only one plot.

It is possible to determine the value of the classical electron radius,  $r_e$ , present in Eq. 2, by fitting the data with the following function:

$$f(\theta) = \phi \cdot n_c \cdot \frac{d\sigma}{d\Omega}(\theta)$$

As in the previously discussed case, three different analyses were performed on the datasets acquired in reflection only, transmission only, and on the combined dataset. The results of these analyses are presented in Fig. 36 and Fig. 37.

It can be observed that the only measurement compatible within  $1\sigma$  with the true value is the one obtained in reflection, while in the other cases the compatibility is at several  $\sigma$ 's.

In Fig. 36, it can be seen that the transmission data appear to exhibit a bias that shifts the data downward along the vertical axis.

A quantitative estimate of this bias can be obtained by performing a fit of the transmission data scaled by a factor  $\alpha$ , as shown in Fig. 38.

To explain the need for this scaling factor, it is necessary to refer to the term  $\wp(\theta; \lambda, \lambda')$ , which, as explained in Appendix D, is calculated by approximating the photon beam as perfectly collimated. This

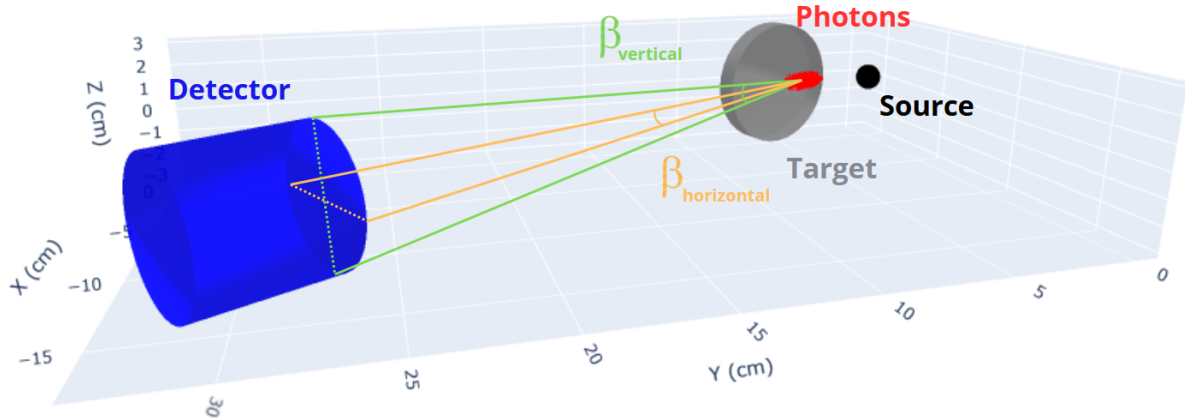


**Fig. 32:** Geometry of the system. We can see the two limit angles defined as  $\beta_{\text{vertical}}$ , in green, and  $\beta_{\text{horizontal}}$ , in orange. The image is produced using the Monte Carlo simulation, more detail in Appendix C.

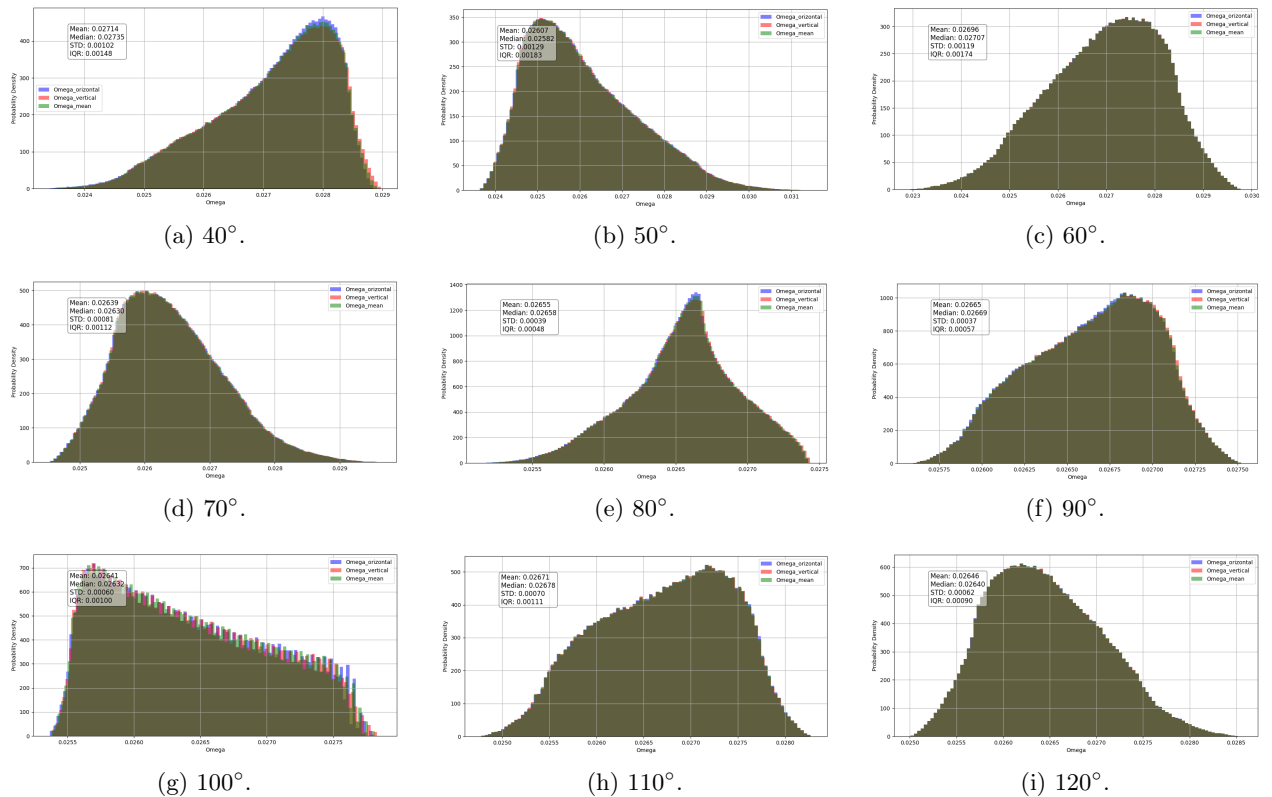


**Fig. 33:** Probability density functions for simulated solid angles in reflection configuration.

represents a rather strong approximation, especially if, as in the present case, the target is kept perpendicular to the axis of the detector used as the gate. The data acquired in reflection do not require

the same correction because, in the calculation of  $\varphi(\theta; \lambda, \lambda')$ , it is assumed that the photon travels the same distance inside the target before and after the scattering. This assumption can be made since the

**Table 7:** Properties of the probability densities for the solid angles in reflection.

Angle (°)	Mean	Median	IQR
40	0.027140	0.027351	0.001477
50	0.026065	0.025820	0.001827
60	0.026961	0.027071	0.001741
70	0.026391	0.026303	0.001117
80	0.026552	0.026576	0.000485
90	0.026651	0.026691	0.000572
100	0.026405	0.026321	0.001001
110	0.026714	0.026775	0.001113
120	0.026458	0.026403	0.000902

**Table 8:** Properties of the probability densities for the solid angles in transmission

Angle (°)	Mean	Median	IQR
35	0.026644	0.026687	0.000844
40	0.027140	0.027351	0.001477
50	0.026065	0.025820	0.001827
60	0.026961	0.027071	0.001741

target was rotated by an angle  $\theta/2$ , where  $\theta$  is the angle at which the measurement is performed, unlike in the transmission framework.

The aforementioned assumption remains valid even in the case of an uncollimated beam.

## 8. Uncertainties

In this section, we outline the methodology used to derive the uncertainty estimates associated with each measured quantity.

### 8.1. Rate uncertainties

Given the formula (Eq. 7) that links the differential cross section to the event rate measured by our experiment, one can write:

$$\frac{1}{\epsilon_{spect}(\theta) \cdot \wp(\theta; \lambda, \lambda')} \frac{dN}{dt d\Omega_{spect}} = \frac{N_{gate}}{T} \cdot n_c \cdot \frac{d\sigma}{d\Omega}$$

one can introduce the shorthand:

$$\begin{aligned} & \frac{1}{\epsilon_{spect}(\theta) \cdot \wp(\theta; \lambda, \lambda')} \frac{dN}{dt d\Omega_{spect}} \approx \\ & \approx \frac{1}{\epsilon_{spect}(\theta) \cdot \wp(\theta; \lambda, \lambda')} \frac{N}{\Delta T \Omega_{spect}} := m \end{aligned}$$

Where  $m$  denotes the measured count density.

With the aforementioned setup, only  $m(\theta)$  was directly recorded,  $\Omega_{spect}$  was subsequently determined via Monte Carlo simulation. Once settled this key concept it is crucial to correctly evaluate the uncertainties linked to these measurements.

#### 8.1.1. Statistical and systematic uncertainties

First, it is essential to distinguish between the various sources of uncertainty encountered in a nuclear physics experiment. In particular one needs to separate the contributions given by *statistical* and *systematic* uncertainties:

- Statistical uncertainties could come from the counting of photons or the errors associated to the fit parameters. These contributions are combined in quadrature.
- Systematic uncertainties stem from various effects, such as the shift of the Compton peak, the errors associated with the geometrical measurements of the apparatus and so on and are likewise summed in quadrature.

To make sure randomness and bias are not mixed together these two kinds of uncertainties will be combined as:

$$\delta_{tot} = \delta_{statistic} \pm \delta_{systematic}$$

where:

$$\delta_{statistic} = \frac{1}{\sqrt{N}} \oplus \left( \frac{\partial m}{\partial N} \right) \delta N$$

$$\begin{aligned} \delta_{systematic} &= \left( \frac{\partial m}{\partial \Omega_{spect}} \right) \delta \Omega_{spect} \oplus \left( \frac{\partial m}{\partial \epsilon_{spect}} \right) \delta \epsilon_{spect} \oplus \\ & \oplus \left( \frac{\partial m}{\partial \wp} \right) \delta \wp \oplus m \left[ \left( \frac{\delta N_{gate}}{N_{gate}} \right) \oplus \left( \frac{\delta n_c}{n_c} \right) \right] \end{aligned}$$

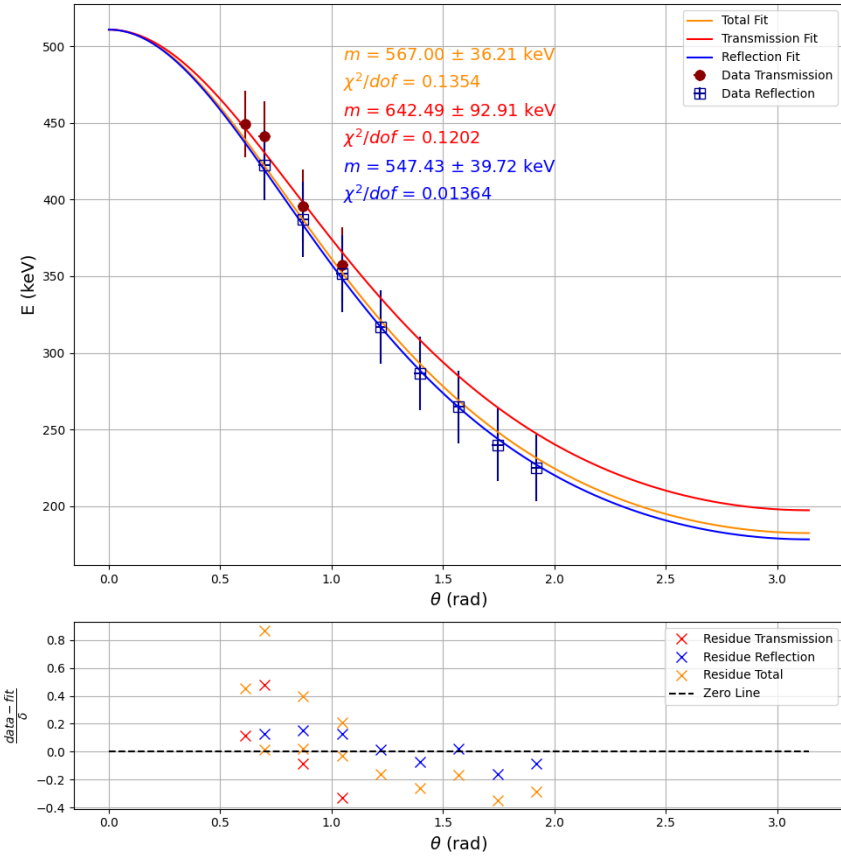
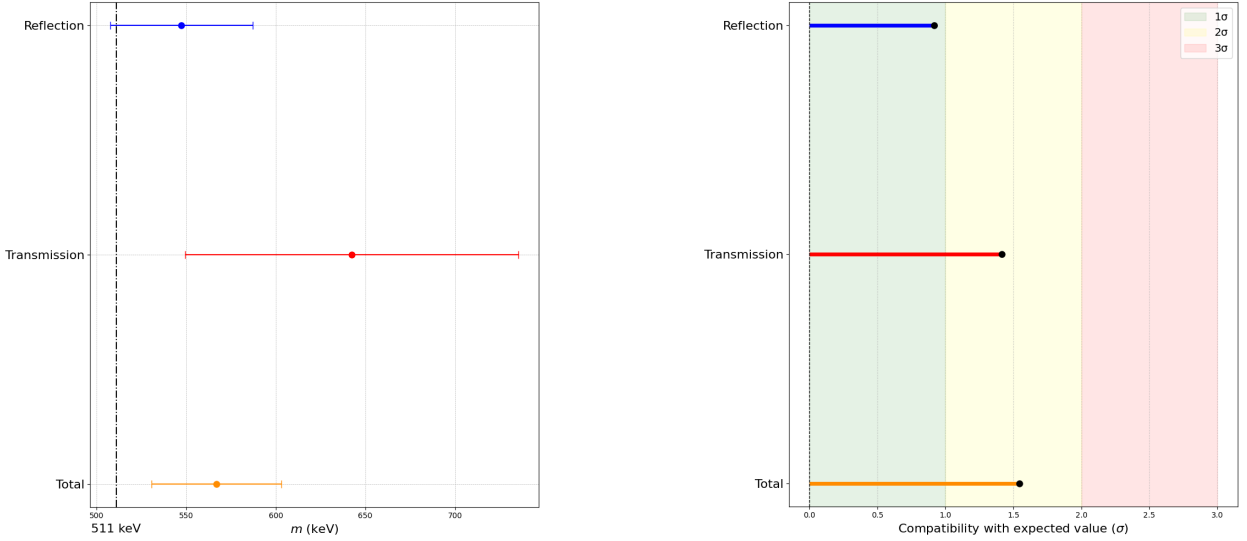


**Fig. 34:** Fit of the energy measurements with the electron mass as a free parameter. The fit for the transmission-only data is shown in red, in blue the fit for the reflection-only data, and in orange the fit for the complete dataset.



(a) Results for the electron mass measurements.  
The black line denote the true value.

(b) Compatibility between the real value and the measured one.

**Fig. 35:** Electron mass results.

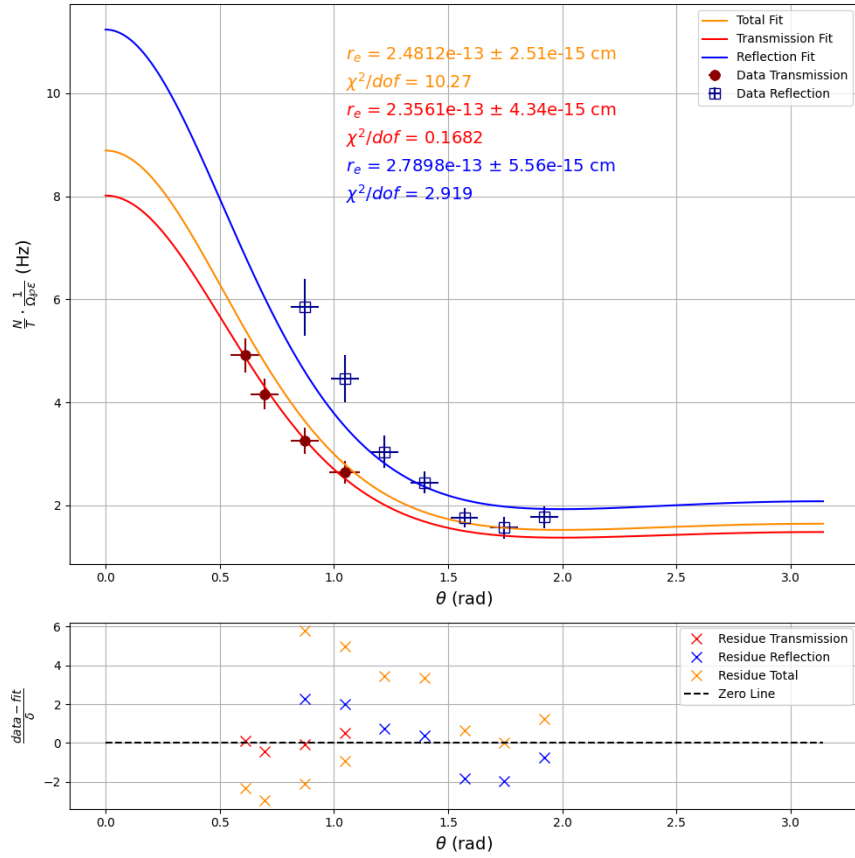
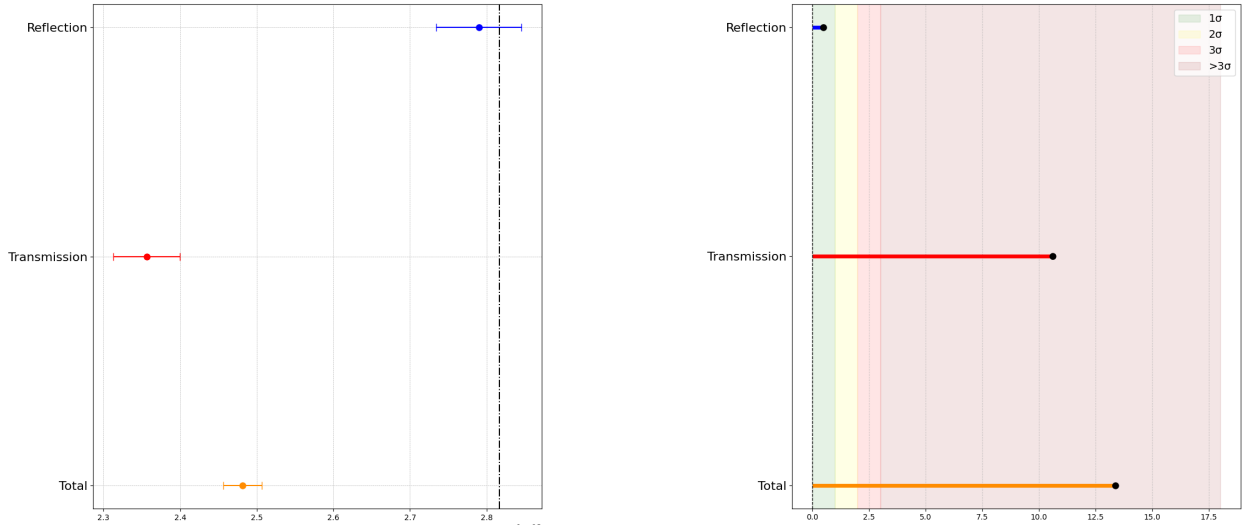


**Fig. 36:** Fit of the energy measurements with the classical electron radius as a free parameter. The fit for the transmission-only data is shown in red, in blue the fit for the reflection-only data, and in orange the fit for the complete dataset.



(a) Results for the classical electron radius measurements. The black line denote the true value.

(b) Compatibility between the real value and the measured one.

**Fig. 37:** Classical electron radius results.

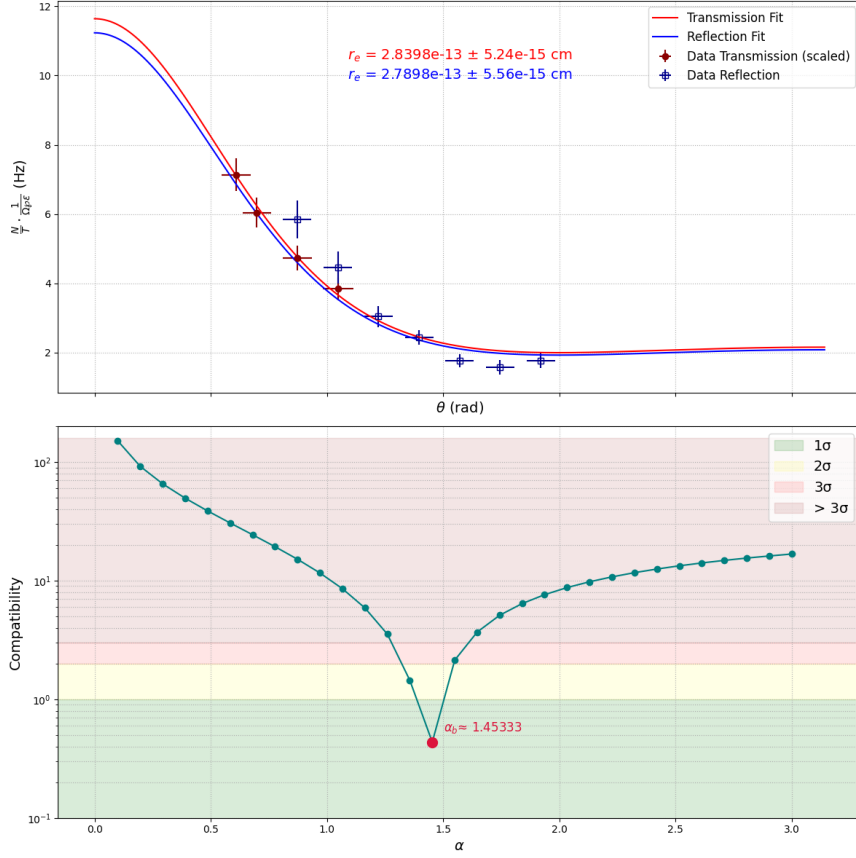


**Fig. 38:** At the top, the fit of the transmission data scaled by the optimal factor,  $\alpha_b$ , is shown. The fit of the unscaled reflection data is also presented, allowing for a direct comparison of the results. At the bottom, the variation of the compatibility of the transmission data fit results as a function of the scaling factor is shown.

assuming every quantity considered in this expression is independent from one another and has a relatively small associated error.

### 8.1.2. $n_c$ and $\varphi$ uncertainties

Given:

$$n_c = \rho \frac{N_a Z}{MM},$$

where:

- $\rho$  is the density of the scattering target,
- $N_a$  is Avogadro's number,
- $MM$  is the target's molar mass,

it follows that each parameter is known to very high precision. Consequently, their uncertainties are negligible and will be omitted from the error analysis. Same goes for the parameter  $\varphi$ .

### 8.1.3. $\epsilon_{spect}$ uncertainty

In this case the value of  $\epsilon_{spect}$  is obtained by interpolation, and its uncertainty is therefore treated as statistical. Given the formula used to fit the efficiency curve:

$$\epsilon_{spect} = A \cdot E^{-B} \cdot \exp(-C \cdot E) + D$$

where  $A, B, C, D$  are all model parameters and  $E$  is the gamma-ray energy. The uncertainty associated to this quantity is propagated in quadrature as:

$$\delta\epsilon = \left( \frac{\partial\epsilon}{\partial A} \cdot \delta A \right) \oplus \left( \frac{\partial\epsilon}{\partial B} \cdot \delta B \right) \oplus \left( \frac{\partial\epsilon}{\partial C} \cdot \delta C \right) \oplus \left( \frac{\partial\epsilon}{\partial D} \cdot \delta D \right)$$

### 8.1.4. $N_{gate}$ uncertainty

Given:

$$N_{gate} = 2 \cdot S(t) \cdot T \cdot BR \cdot \frac{\Delta\Omega}{4\pi} \cdot \epsilon_{gate} \quad (511)$$

where:

- $S(t)$  is the source activity in becquerels (Bq),
- $T$  is the acquisition time,
- BR is the branching ratio for the 511 keV photon,
- $\frac{\Delta\Omega}{4\pi}$  is the solid angle subtended by the detector,
- $\epsilon_{gate}(511)$  is the gate detector efficiency for a 511 keV photon,

in this case one can assume that the branching ratio (BR) is known with high precision and the acquisition time ( $T$ ) is treated as error-free, since it is controlled within the Maestro software. The uncertainties in  $S(t)$  and  $\epsilon_{gate}$  are treated as statistical and the one associated to  $\Delta\Omega$  is systematic.

- **$\delta S(t)$  computation:**

As shown in Section 4.6, the uncertainty on this value is:

$$\delta S(t) = 11647 \text{ Bq}.$$

- **$\delta\epsilon_{gate}$  computation:**

For this computation please refer to Section 8.1.3. By assigning a 2.5% error on each point, from the linear fit the following uncertainty is obtained:

$$\delta\epsilon_{gate}(511) = 0.01672$$

- **$\delta(\Delta\Omega/4\pi)$  computation:**

To evaluate the uncertainty in the gate's solid-angle fraction one can start from:

$$\frac{\Delta\Omega}{4\pi} = \frac{1 - \cos(\beta)}{2}$$

where  $\beta$  is computed as:

$$\beta = \arctan\left(\frac{r_{gate}}{d_{source-gate}}\right).$$

Both of these two measurements are known with their uncertainty,  $r_{gate} = (1, 27 \pm 0, 01) \text{ cm}$  and  $d_{source-gate} = d = (18.54 \pm 0.5) \text{ cm}$ . Propagating these uncertainties in quadrature gives:

$$(\delta(\Delta\Omega/4\pi)) = \left(\frac{\partial(\Delta\Omega/4\pi)}{\partial r}\delta r\right) \oplus \left(\frac{\partial(\Delta\Omega/4\pi)}{\partial d}\delta d\right)$$

Substituting  $r$ ,  $d$ , and their uncertainties yields the numerical value of  $\delta(\Delta\Omega/4\pi)$ .

$$\delta(\Delta\Omega/4\pi) = 6.54 \cdot 10^{-5}$$

### 8.1.5. $d\Omega_{spect}$ uncertainty

To calculate the solid angle subtended by the detector used as a spectrometer, a Monte Carlo simulation was employed, as described in Section 6.5. An uncertainty was associated with this measurement, derived from the interquartile range (IQR), which is an appropriate estimator for non-symmetric probability distributions due to its robustness against outliers.

### 8.1.6. Total uncertainties

With these definitions, the total uncertainty on the rate measurement can be expressed as:

$$\delta m = \delta_{statistic} \pm \delta_{systematic}$$

## 8.2. Angle uncertainties

On the x-axis of the Klein-Nishina plot, we report the scattering angles. Several sources of uncertainty are associated with these quantities, including:

- The shift in the position of the Compton peak due to temperature instabilities and other environmental factors.
- The error associated with the measurement of the scattering angle.
- The uncertainty linked to the spectrometer resolution, which is not ideal.
- The statistical error derived from the Gaussian fit of the Compton peak.

While these first three factors have a systematic nature, the last one can be considered as strictly statistical. Knowing this it is crucial to transform every energy-related quantity into an angle-related quantity. This can be done by using the inverted Compton formula shown below:

$$\theta(E') = \arccos\left[2 - \frac{511}{E'}\right]$$

which leads to the following associated uncertainty expression:

$$\delta\theta = \left| \frac{511}{E'^2 \cdot \sqrt{1 - (2 - \frac{511}{E'})^2}} \right| \cdot \delta E'$$

### 8.2.1. Peak shift uncertainty

Given that the Compton peak undergoes a mean fluctuation  $\Delta E_{peak} = 8 \text{ ch} = 24 \text{ keV}$ , we used  $\delta E_{peak} = \frac{\Delta E_{peak}}{2} = 4 \text{ ch} = 12 \text{ keV}$  to quantify our peak energy uncertainty. This can be expressed as:

$$\delta\theta_{peak} = \left| \frac{511}{E'^2 \cdot \sqrt{1 - (2 - \frac{511}{E'})^2}} \right| \cdot \delta E_{peak}.$$

### 8.2.2. Scattering angle uncertainty

This is chosen based on the instrumental error used to measure  $\theta_{scattering}$ , and it is called  $\delta\theta_{scattering}$ . Assuming:

$$a = \arctan \left( \frac{r_{spectrometer}}{d_{target-spectrometer}} \right)$$

the error associated to the placement of the detector at a given scattering angle can be computed as:

$$\delta\theta_{scattering} = \frac{a}{\sqrt{12}}$$

### 8.2.3. Resolution uncertainty

The uncertainty associated with the resolution of a detector can be expressed using the percent resolution of the spectrometer, which can be computed as:

$$\delta_{resolution} = \frac{2.35 \cdot \sigma_{fit}}{channel} \cdot 100$$

As in the previous case, this quantity needs to be expressed in terms of the scattering angle. This can be computed using:

$$\delta\theta_{resolution} = \left| \frac{511}{\sin\theta \cdot (E')^2} \right| \cdot \delta_{resolution}$$

### 8.2.4. Statistical uncertainty

The uncertainty arising solely from the fit of the Compton peak can be accounted for using the formula:

$$\delta_{fit} = \frac{\sigma_{fit}}{\sqrt{N}}$$

where N is the number of counts within the Compton peak. As in previous cases, this uncertainty must also be expressed in terms of the scattering angle. Using the same transformation, we obtain:

$$\delta\theta_{fit} = \left| \frac{511}{\sin\theta \cdot (E')^2} \right| \cdot \delta_{fit}.$$

### 8.2.5. Final results

The error bars on the x-axis can be expressed as a sum of statistical and systematic uncertainties following:

$$\delta\theta = \delta\theta_{stat} \pm \delta\theta_{syst}$$

$$= (\delta\theta_{fit}) \pm (\delta\theta_{peak} \oplus \delta\theta_{scattering} \oplus \delta\theta_{resolution})$$

## 8.3. Energy uncertainties

In the plot presented in Section 7.1, we have made use of the measured energy at which the Compton peak occurs. An uncertainty is associated with this measurement, arising from the combination of several factors: the Compton-peak shift, the energy resolution of the apparatus, and the statistical uncertainty from the fit performed on the peak. These sources of uncertainty were discussed in detail in Section 8.2 and have been combined according to the following expression:

$$\delta E = \delta E_{shift} \pm (\delta E_{resolution} \oplus \delta E_{fit})$$

## 9. Conclusion of the Experiment

In this work, we set up and characterized an experimental apparatus to study Compton scattering on a copper target, using a 2" NaI(Tl) scintillation detector in coincidence with a gating detector to select scattering events.

### 9.1. Main results

The main results are summarized as follows:

- **Efficiency and stability:** analysis of ADC linearity, temporal stability, and calibration confirm a stable and linear detector response within experimental uncertainties. Detector efficiencies were verified using standard gamma sources and found to be consistent with tabulated expectations.
- **Electron mass:** extracted by fitting the variation of the scattered photon energy as a function of angle, shows good agreement with the theoretical value  $m_e = 511 \text{ keV}/c^2$ . All three analysis (reflection, transmission, and combined dataset) are consistent within  $2\sigma$ , with the reflection dataset yielding the most precise measurement.
- **Classical electron radius:** obtained by fitting the angular dependence of normalized count rates. Only the reflection dataset yielded a result consistent within  $1\sigma$  with the true value, while the transmission data exhibited a systematic deviation, attributable to the approximation of a perfectly collimated beam in the term  $\wp(\theta; \lambda, \lambda')$ , later corrected using an empirical scaling factor  $\alpha$ .

### 9.2. Main experimental limits

The main experimental limitations identified were:

- 
- **Beam collimation:** the ideal beam approximation introduced a bias in the  $\phi$  function, especially in the transmission framework. As suggested in the literature, rotating the target by  $\theta/2$  in transmission as well would help improve the symmetry and accuracy of  $\phi$ .
  - **Geometry constraints:** spatial and angular limitations led to suboptimal distances between the source, target, and spectrometer, slightly reducing energy resolution and counting statistics.
  - **Gain stability:** slow gain shifts and peak drifts require further investigation into temperature effects and stabilization time to reduce systematic uncertainties.

### 9.3. Future improvements

For future improvements, we recommend:

1. Adopting the reflection-like geometry (target inclined by  $\theta/2$ ) also for transmission measurements, to improve the reliability of  $\phi(\theta; \lambda, \lambda')$ ,
2. Implementing fine collimation or a remotely controlled rotation system for more accurate angular alignment,
3. Extending acquisition and monitoring times to identify fully stationary operation regimes.

With these optimizations, the apparatus could provide even more accurate and precise measurements of the electron mass and classical radius, approaching the precision of reference international values.

## A. Scintillators

[11] During the experiment, two NaI(Tl) detectors were used to perform the measurements; a brief description of their operation is provided below. Scintillators are devices based on a relatively simple principle: an ionizing particle deposits energy in the material, causing atomic excitations. The subsequent de-excitation of these states produces photons that can be detected once the scintillator is coupled to a photomultiplier tube. In our case, inorganic scintillators were used. These are typically crystals (NaI, CsI, BGO) specifically designed to convert the released energy into visible light. These materials have a high light yield but exhibit relatively slow response times (on the order of 100 ns). When energy is deposited in the material, electrons are excited from the valence band (*VB*) to the conduction band (*CB*), creating a hole. This process is only possible if the energy given to the electron exceeds the bandgap energy ( $E_g$ ), i.e., the energy separating the *CB* from the *VB*. The excited electron tends to relax back to the bottom of the *CB*, with a subsequent recombination in the *VB* that emits photons. However, if the emission spectrum coincides with the absorption spectrum, the material is opaque to its own produced light, making it inefficient for detection. To overcome this problem, known as self-absorption, it is common practice to use dopants that ensure the emission and absorption spectra do not overlap, allowing for fast and transparent re-emission that facilitates light collection. The fluorescence of NaI(Tl) is characterized by a primary decay time of about 230 ns. There is also a slower component (phosphorescence), due to the presence of trapping centres that delay photons on the scale of a few microseconds. Although these response times are longer than those of organic scintillators, they are compensated by a high light yield (up to  $\sim 38000$  photons/MeV) and good energy resolution (approximately 7% @ 662 keV of  $^{137}\text{Cs}$ ). Thanks to their high density and high atomic number, inorganic scintillators are particularly suitable for detecting charged particles or photons, for which the photoelectric effect and Compton scattering dominate the cross section.

## B. Compton Theory

All calculations in this section are carried out in Natural Units (NU) [19].

### B.1. Compton Scattering

The Compton effect describes the scattering of a photon off a free electron, resulting in an increase in the wavelength of the scattered photon.

The relation governing this phenomenon is:

$$\lambda' - \lambda = \frac{1}{m} (1 - \cos \theta)$$

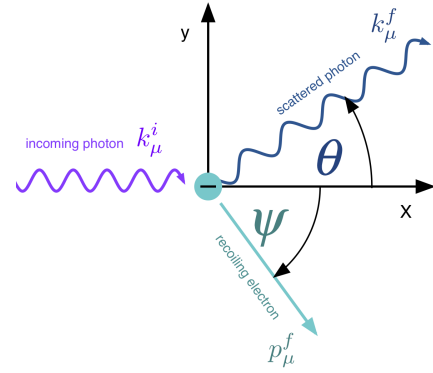


**Fig. 39:** Simplified schematic of a Compton scattering event [20].

where:

- $\lambda$  and  $\lambda'$  are the incident and scattered photon wavelengths, respectively;
- $m$  is the electron mass;
- $\theta$  is the photon scattering angle.

To derive it, referring to Fig. 39, we impose conservation of energy and momentum in the scattering process.

Photon energies are given by the Planck relation:

$$E = \frac{1}{\lambda}, \quad E' = \frac{1}{\lambda'}.$$

Total energy before and after scattering must include the electron's rest energy:

$$\frac{1}{\lambda} + m = \frac{1}{\lambda'} + \gamma m,$$

where  $\gamma$  is the Lorentz factor of the electron after collision.

From de Broglie's relation:

$$p = \frac{1}{\lambda}.$$

Applying momentum conservation in the horizontal and vertical directions gives:

$$\begin{cases} \frac{1}{\lambda} = \frac{1}{\lambda'} \cos \theta + \gamma m v \cos \psi, \\ 0 = \frac{1}{\lambda'} \sin \theta - \gamma m v \sin \psi. \end{cases}$$

After some algebraic manipulation, one obtains:

$$\lambda' - \lambda = \frac{1}{m} (1 - \cos \theta).$$

Finally, using the definition of  $E'$  above, the scattered photon energy can be written as:

$$E' = \frac{E}{1 + \frac{E}{m} (1 - \cos \theta)}.$$

## B.2. Compton Cross-Section

The most general expression for a scattering process involving  $i$  incoming particles and  $f$  outgoing particles is given by the following relation [19]:

$$d\sigma = \frac{(2\pi)^4}{v_{\text{rel}}} \cdot \delta^4 \left( \sum_i p_i - \sum_f p_f \right) \cdot \prod_i \left( \frac{m_i}{E_i} \right) \cdot \prod_f \left( \frac{m_f}{E_f} \right) \cdot |\mathcal{M}|^2 \cdot \prod_f \frac{d^3 p_f}{(2\pi)^3}$$

where:

- $v_{\text{rel}}$  is the relative velocity between incoming particles;
- $\delta^4$  is the Dirac delta in Minkowski space;
- $\mathcal{M}$  is the Feynman matrix element;
- $\prod_f \frac{d^3 p_f}{(2\pi)^3}$  represents the phase space volume element.

In the case of Compton scattering:

$$e^-(p) + \gamma(k) \rightarrow e^-(p') + \gamma(k'),$$

the cross-section can be rewritten as:

$$d\sigma = \frac{(2\pi)^4 m^2}{4(E_p \omega_k) v_{\text{rel}}} \cdot \delta^4(p + k - p' - k') \cdot |\mathcal{M}|^2 \cdot \frac{d^3 p_{p'}}{(2\pi)^3 2E_{p'}} \cdot \frac{d^3 p_{k'}}{(2\pi)^3 2\omega_{k'}}$$

We begin by analyzing the kinematic part of the cross-section. By integrating the  $\delta^3$  function over the outgoing electron momentum and rewriting the photon's momentum in cylindrical coordinates, we obtain:

$$d\sigma = \frac{4m^2}{64\pi^2(E_p \omega_k E_{p'}) v_{\text{rel}}} \cdot \delta(E_p + \omega_k - E_{p'} - \omega_{k'}) \cdot |\mathcal{M}|^2 \cdot \frac{p_{k'}^2 d\Omega'}{\omega_{k'}}$$

It can be shown that in the laboratory frame  $v_{\text{rel}} = 1$ . The remaining Dirac delta can then be rewritten in terms of  $\omega_{k'}$  to allow further integration.

Altogether, we arrive at the following expression for the differential cross-section:

$$\frac{d\sigma}{d\Omega'} = \frac{1}{(4\pi)^2} \left( \frac{\omega'}{\omega} \right)^2 \cdot |\mathcal{M}|^2 \quad (9)$$

It remains to compute the matrix element, which involves evaluating two Feynman diagrams, as shown in Fig. 40.

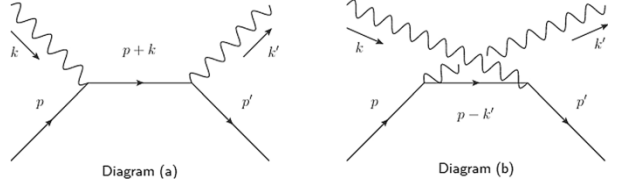


**Fig. 40:** Feynman diagrams for the Compton scattering process at Leading Order. [21]

$$|\mathcal{M}|^2 = \frac{1}{4} \sum_{\text{spins}} \left[ |\mathcal{M}_{(a)}|^2 + |\mathcal{M}_{(b)}|^2 + \mathcal{M}_{(a)}^{\mu\nu} \mathcal{M}_{(b)}^{*\mu\nu} + \mathcal{M}_{(a)}^{*\mu\nu} \mathcal{M}_{(b)}^{\mu\nu} \right] \quad (10)$$

The first term can be explicitly written as:

$$|\mathcal{M}_{(a)}|^2 = \left[ \bar{u}(p') i e \gamma^\mu \cdot \frac{i}{f_1 - m} \cdot i e \gamma^\nu u(p) \right] \cdot \left[ \bar{u}(p) i e \gamma_\nu \cdot \frac{i}{f_1 - m} \cdot i e \gamma_\mu u(p') \right]$$

where  $f_1 = p + k$ .

The remaining terms of the matrix element can be written analogously.

By computing all terms in Eq. (10), one obtains:

$$|\mathcal{M}|^2 = \alpha^2 \left[ \frac{\omega'}{\omega} + \frac{\omega}{\omega'} - \sin^2 \theta \right]$$

Putting all together, we arrive at the Klein–Nishina formula for the differential cross-section:

$$\frac{d\sigma}{d\Omega'} = \frac{\alpha^2}{(4\pi)^2} \left( \frac{\omega'}{\omega} \right)^2 \cdot \left[ \frac{\omega'}{\omega} + \frac{\omega}{\omega'} - \sin^2 \theta \right]$$

## C. Monte Carlo Simulation

A numerical simulation written in Python was used to carry out some studies. This section aims to present how the simulation works; for more details, please refer to the dedicated section on the GitHub profile.

### C.1. Photon Interaction Types

The simulation framework models gamma-ray interactions specifically for low-energy photons characteristic of the  $^{22}\text{Na}$  spectrum. This radioactive isotope decays via beta-plus ( $\beta^+$ ) decay, producing a positron that subsequently annihilates with an electron, emitting two 511 keV gamma photons in opposite directions. Additionally,  $^{22}\text{Na}$  emits a 1274 keV gamma photon following its decay to an excited state of  $^{22}\text{Ne}$ .

Given the energy range of interest, the simulation focuses on two dominant interaction processes: Compton scattering and photoelectric effect, omitting pair production due to its higher energy threshold.

## C.2. Implemented cross-section

### C.2.1. Thomson scattering cross-section

A significant value is the Thomson scattering cross-section, and is given by:

$$\sigma_T = \frac{8}{3}\pi r_e^2$$

Where  $r_e = 2.817 \cdot 10^{-15}$  m is the classical electron radius.

### C.2.2. Photoelectric Effect cross-section

The cross-section for the photoelectric effect is computed using a formula involving the atomic number of the detector material and the photon's energy. [22]

The Photoelectric cross-section is computed using:

$$\sigma_{pe} = c \left( \frac{Zm_e}{E_\gamma} \right)^5 (\gamma^2 - 1)^{3/2} \left[ \frac{4}{3} + \frac{\gamma(\gamma - 2)}{\gamma + 1} \cdot \left( 1 - \frac{1}{2\gamma\sqrt{\gamma^2 - 1}} \ln \left( \frac{\gamma + \sqrt{\gamma^2 - 1}}{\gamma - \sqrt{\gamma^2 - 1}} \right) \right) \right]$$

where:

- $c = \frac{3}{2}\alpha^4\sigma_T$ .
- $\gamma = \frac{E_\gamma + m_e - E_b}{m_e}$ .
- $E_\gamma$  is the photon energy.
- $m_e = 511$  keV is the electron rest mass energy.
- $E_b \approx 0$  is the bond energy for the electron.
- $Z$  is the atomic number.
- $\alpha \approx \frac{1}{137}$  is the fine-structure constant.

### C.2.3. Compton Scattering cross-section

The cross-section for Compton scattering is computed based on the Thomson scattering cross-section and other parameters like the photon energy and the scattering angle. [22]

The Compton cross-section is computed using:  
if  $E > 100$  keV:

$$\sigma_C = cZ \left[ \frac{(1+\epsilon)}{\epsilon^2} \left( \frac{2(1+\epsilon)}{1+2\epsilon} - \frac{\ln(1+2\epsilon)}{\epsilon} \right) + \frac{\ln(1+2\epsilon)}{2\epsilon} - \frac{1+3\epsilon}{(1+2\epsilon)^2} \right]$$

where:

- $c = \frac{3}{4}\sigma_T$ .
- $\epsilon = \frac{E_\gamma}{m_e}$ .
- $E_\gamma$  is the photon energy.
- $m_e = 511$  keV is the electron rest mass energy.

if  $E < 100$  keV:

$$\sigma_C = \sigma_T Z \left[ \frac{1}{(1+2\epsilon)^2} \left( 1 + 2\epsilon + \frac{6}{5}\epsilon^2 - \frac{1}{2}\epsilon^3 + \frac{2}{7}\epsilon^4 - \frac{6}{35}\epsilon^5 + \frac{8}{105}\epsilon^6 + \frac{4}{105}\epsilon^7 \right) \right]$$

## C.3. Interaction Probability and Attenuation

The probability of interaction for a photon travelling through a material depends on the total cross-section and material properties such as density and molar mass. This is calculated in two steps:

### C.3.1. Attenuation Factor

The attenuation factor is defined as the inverse of the photon's mean free path in the material:

$$\mu = \frac{\rho \cdot N_a}{MM} \cdot \sigma_{tot}$$

where:

- $N_a = 6.022 \cdot 10^{23}$  mol<sup>-1</sup> is the Avogadro's number.
- $\rho$  is the density (in g/cm<sup>3</sup>) of the scattering material.
- MM is the molar mass (in g/mol) of the scattering material.
- $\sigma_{tot}$  is the total cross section, calculated combining the contributions of the photoelectric and Compton cross-sections.

### C.3.2. Interaction Probability

Using the attenuation factor, the probability of photon interaction after travelling a distance  $d$  in the material is:

$$I = 1 - e^{-\mu d}$$

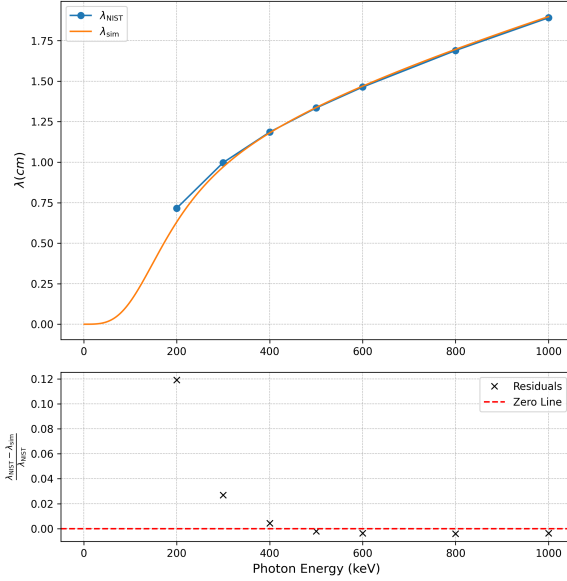


**Fig. 41:** Comparison of the attenuation length for energies between [200, 1000] keV

#### C.4. Comparison with NIST data

In order to have a validation for this Monte Carlo simulation we compare the attenuation length,  $\lambda$  for different energies.

$$\lambda = \frac{1}{\mu}$$

We can observe in the Figure 41, that for the range of energies between [200, 1000] keV, we find an error that is never bigger than 12% and in particular for energies very close to 511 keV, the precision of the simulation is very high, under 1%.

#### D. Relationship Between Cross-section and Count Rate

To derive Eq. 7, which connects the measured count rate to the value of the cross-section, we begin by rewriting it as:

$$\frac{dR}{d\Omega} = \underbrace{\epsilon_{\text{spect}} N_c \Phi}_{C} \frac{d\sigma}{d\Omega}$$

Here,  $N_c$  represents the number of available scattering centres, and  $\Phi$  the incident photon flux. Recalling Section 6.1, we can express:

$$N_c = n_c V$$

where  $V$  is the volume of the illuminated portion of the target.

As for  $\Phi$ , we want to study the photon flux that interacts within a specific slice of the target at depth

$(x, x + dx)$ :

$$\Phi = \underbrace{\frac{N_{\text{gate}}}{T}}_{\phi_{\text{gate}}} \cdot \frac{1}{A} \cdot e^{-x/\lambda} \cdot e^{-l/\lambda'}$$

Here,  $A$  is the area illuminated at depth  $x$ , while the exponential terms express the probability that photons in the beam do not undergo Compton scattering before depth  $x$  ( $e^{-x/\lambda}$ ) and do not undergo further scattering along the remaining path  $l$  ( $e^{-l/\lambda'}$ ). Since we are analysing only a thin layer at depth  $(x, x + dx)$ , the illuminated volume can be written as:

$$dV = Adx$$

Putting this together, the term  $\mathcal{C}$  becomes:

$$\mathcal{C} = \epsilon_{\text{spect}} \cdot n_c \cdot \phi_{\text{gate}} \cdot \underbrace{\int_0^{d_{\max}} dx e^{-x/\lambda} e^{-l/\lambda'}}_{\wp(\theta; \lambda, \lambda')} \quad (11)$$

The term  $\wp(\theta; \lambda, \lambda')$  depends on the geometry used in the experiment.

#### D.1. Transmission

To calculate the factor  $\wp(\theta; \lambda, \lambda')$  in this case, we evaluate the integral in Eq. 11 using the appropriate expressions for  $d_{\max}$  and  $l$ . Assuming a perfectly collimated beam, we have:

$$d_{\max} = D, \quad l = \frac{D - x}{\cos \theta}$$

where  $D$  is the total thickness of the target. See Fig. 23 for a schematic.

Solving the integral yields:

$$\wp(\theta; \lambda, \lambda') = \lambda_T \cdot e^{-D/(\lambda' \cos \theta)} \cdot \left( 1 - e^{-D/\lambda_T} \right)$$

where:

$$\frac{1}{\lambda_T} = \frac{1}{\lambda} - \frac{1}{\lambda' \cos \theta}$$

Note that the above formula diverges for  $\theta = \pi/2$ . This is not problematic for the measurements discussed, as only angles below 70° were explored in this configuration.

#### D.2. Reflection

The reflection geometry is shown in Fig. 19. In this case, the assumption of a perfectly collimated beam implies that the triangle formed by the interaction point and the entry and exit points in the target is isosceles. Therefore, the distance travelled after the first scattering equals  $x$ , and we have:

$$d_{\max} = D' = \frac{D}{\cos(\frac{\pi-\theta}{2})}, \quad l = x$$

Substituting these into the formula yields:

$$\wp(\theta; \lambda, \lambda') = \lambda_R \cdot \left(1 - e^{-D'/\lambda_R}\right)$$

where:

$$\frac{1}{\lambda_R} = \frac{1}{\lambda} + \frac{1}{\lambda'}$$

## E. Optimal Thickness Calculation

To determine the optimal target thickness, we differentiate the factor  $\wp(\theta; \lambda, \lambda')$  (derived in Appendix D) with respect to  $D$  and solve for the zero of the resulting expression.

### E.1. Transmission

$$\begin{aligned} \frac{d\wp}{dD} &= \lambda_T e^{-\frac{D}{\lambda' \cos \theta}} \left[ -\frac{1}{\lambda' \cos \theta} + \right. \\ &\quad \left. + \left( \frac{1}{\lambda' \cos \theta} + \frac{1}{\lambda_T} \right) e^{-\frac{D}{\lambda_T}} \right] \end{aligned}$$

We now find the value of  $D$  that makes the square bracket vanish:

$$-\frac{1}{\lambda' \cos \theta} + \frac{\lambda_T + \lambda' \cos \theta}{\lambda_T \lambda' \cos \theta} e^{-D/\lambda_T} = 0$$

Rearranging terms:

$$e^{-D/\lambda_T} = \frac{\lambda_T}{\lambda_T + \lambda' \cos \theta}$$

$$D = \lambda_T \ln \left( \frac{\lambda_T + \lambda' \cos \theta}{\lambda_T} \right)$$

### E.2. Reflection

$$\frac{d\wp}{dD} = e^{-\frac{D'}{\lambda_R}} \frac{dD'}{dD} = \frac{1}{\cos(\frac{\pi-\theta}{2})} e^{-D'/\lambda_R}$$

This derivative becomes zero only when the exponential term vanishes, which happens if and only if  $D' \rightarrow \infty$ . Given that the denominator of  $D'/\cos(\frac{\pi-\theta}{2})$  cannot vanish by construction, this condition is satisfied only in the limit  $D \rightarrow \infty$ .

## F. Figures

### F.1. Electronic Chain



**Fig. 42:** Final readout chain of the Compton apparatus. From right to left: NIM-TTL-NIM converter, Dual Timer, TSCA, AMP and Power Supply.

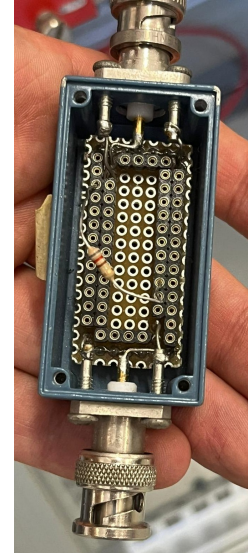


**Fig. 43:** A  $384 \Omega$  resistor connected in parallel to the AMP, used to simulate the voltage drop in the auto-coincidence setup.

## F.2. Apparatus

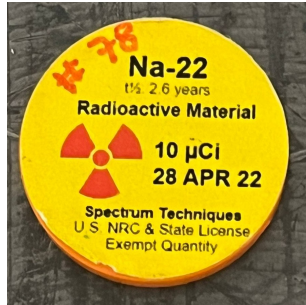


**Fig. 44:** The  $^{22}\text{Na}$  source used throughout the experiment.



**Fig. 47:** Close-up of the apparatus section dedicated to the spectrometer.

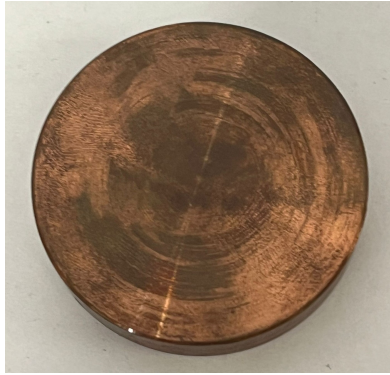


**Fig. 45:** Copper target with a thickness of 1 cm and a diameter of 5 cm used as a scattering medium.

## F.3. Measurements

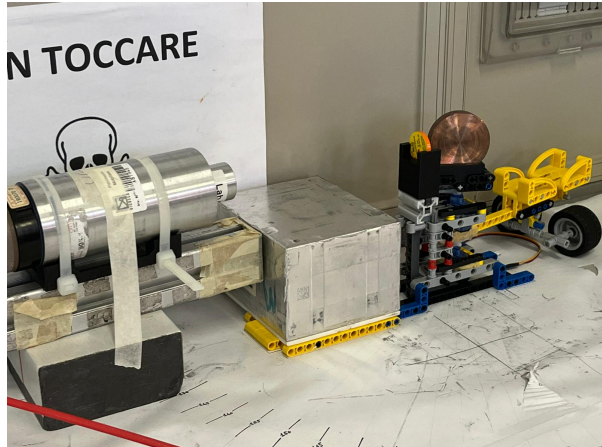


**Fig. 46:** Close-up of the apparatus section dedicated to gate generation.

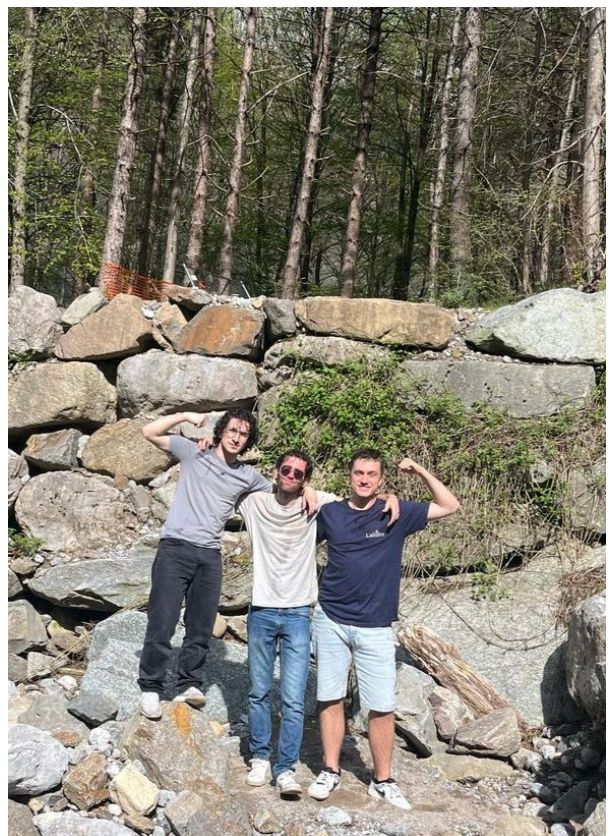


**Fig. 48:** "Knowledge flows like a river: always changing and transient; but lived experience and true bonds etch themselves into the soul, enduring beyond the wear of days." ~ Eracrito.

---

## References

- [1] ORTEC. *905 Series NaI(Tl) Scintillation Detectors*. Model 905. Oak Ridge, TN, USA, 2013.
- [2] Scionix Holland B.V. *2x2 NaI(Tl) Detector*. Model 2x2. Bunnik, Paesi Bassi, 2024.
- [3] ORTEC. *Model 276 Photomultiplier Base with Preamplifier*. ORTEC, AMETEK Advanced Measurement Technology, Inc. Oak Ridge, TN, USA, 2007.
- [4] SCIONIX Holland BV. *Voltage Dividers and Electronics for Scintillation Detectors*. SCIONIX Holland BV. Bunnik, The Netherlands, 2013.
- [5] ORTEC. *572A Amplifier*. Model 572A. Oak Ridge, TN, USA, n.d.
- [6] ORTEC. *ORTEC 590A Amplifier and Timing Single-Channel Analyzer*. Instruction manual for the ORTEC Model 590A. Oak Ridge, TN, USA, 2007.
- [7] ORTEC. *MAESTRO V7 Multichannel Analyzer Software*. Product leaflet for MAESTRO V7 software. Oak Ridge, TN, USA, Aug. 2012.
- [8] CAEN S.p.A. *A7585 - DT5485P Digital Controlled SiPM Power Supplies User's Manual*. Rev. 2. User manual for installation, configuration, and use of SiPM power supply modules. CAEN Electronic Instrumentation. Via Vetraia, 11, 55049 Viareggio (LU), Italy, June 2019. URL: <https://www.caen.it>.
- [9] CAEN. *Manual for Dual Timer: caenN93B*. Model: caenN93B. CAEN. Viareggio, Italia, n.d..
- [10] CAEN. *Manual for NIM-TTL-NIM : caenN89*. Model: caenN89. CAEN. Viareggio, Italia, n.d..
- [11] Glenn F Knoll. *Radiation detection and measurement*. New York, NY: Wiley, 2010. URL: <https://cds.cern.ch/record/1300754>.
- [12] ORTEC. *Electronics Standards and Definitions: NIM and CAMAC Standards for Modular Instrumentation*. Oak Ridge, TN, USA, n.d.
- [13] Christopher Charles Busby. "The Secondary Photoelectron Effect: Gamma Ray Ionisation Enhancement in Tissues from High Atomic Number Elements". In: *Use of Gamma Radiation Techniques in Peaceful Applications*. Ed. by Basim A. Almayah. Rijeka: IntechOpen, 2019. Chap. 11. DOI: 10.5772/intechopen.86779. URL: <https://doi.org/10.5772/intechopen.86779>.
- [14] Paul Adamson. "A general quantum mechanical method to predict positron spectroscopy". In: (Jan. 2007).
- [15] G. Gervasio L. Zanotti A. Alessandrello. "Misura della diffusione Compton in un esperimento a scopo didattico". In: *Giornale di fisica* 35.3 (1994). INFN sezione MI, pp. 193–204.
- [16] Wikipedia contributors. *Cobalt-60 Decay Scheme*. [https://it.m.wikipedia.org/wiki/File:Cobalt-60\\_Decay\\_Scheme.svg](https://it.m.wikipedia.org/wiki/File:Cobalt-60_Decay_Scheme.svg). Accessed: 2025-07-07. 2024.
- [17] ORTEC. *Experiment 3.6: Activity of a Gamma Emitter (Absolute Method)*. Gamma-Ray Spectroscopy Using NaI(Tl). 2007. URL: <https://www.ortec-online.com/>.
- [18] Wikipedia contributors. *Law of cosines — Wikipedia, The Free Encyclopedia*. Accessed: 2025-07-03. 2024. URL: [https://en.wikipedia.org/wiki/Law\\_of\\_cosines](https://en.wikipedia.org/wiki/Law_of_cosines).
- [19] Francesco Terranova. *A Modern Primer in Particle and Nuclear Physics*. Oxford University Press, Nov. 2021. ISBN: 978-0-19-284524-5, 978-0-19-284525-2.
- [20] PhysicsOpenLab. *Compton Scattering*. 2016. URL: <https://physicsopenlab.org/2016/02/04/compton-scattering-2/>.
- [21] D. S. Cabral and A. F. Santos. "Compton scattering in TFD formalism". In: *The European Physical Journal C* 83.25 (2023). DOI: 10.1140/epjc/s10052-023-11182-x. URL: <https://doi.org/10.1140/epjc/s10052-023-11182-x>.
- [22] Wikipedia contributors. *Cross-section formulas*. URL: [https://en.wikipedia.org/wiki/Gamma\\_ray\\_cross\\_section](https://en.wikipedia.org/wiki/Gamma_ray_cross_section).